https://ntrs.nasa.gov/search.jsp?R=20170003155 2018-07-23T22:54:32+00:00Z

Small-scale density variations in the lunar crust revealed by GRAIL

J. C. Jansen[1], J. C. Andrews-Hanna[2], Y. Li[1], P. G. Lucey[3], G. J. Taylor[3], S. Goossens[4], F. G. Lemoine[4], E. Mazarico[4], J. W. Head III[5], C. Milbury[6], W. S. Kiefer[7], J. M. Soderblom[8], and M. T. Zuber[8]

In preparation for submission to Icarus

May 9, 2016

[1]Department of Geophysics, Colorado School of Mines, Golden, CO 80401, jjansen@mines.edu, [2]Southwest Research Institute, Boulder, CO 80302, [3]Hawaii Institute of Geophysics and Planetology, University of Hawaii, Honolulu, HI 96822, [4]NASA Goddard Space Flight Center, Greenbelt, MD 20771, [5]Department of Geological Sciences, Brown University, Providence, RI 02912, [6]Purdue University. West Lafayette, IN 47907, [7]Lunar and Planetary Institute, Houston TX 77058, [8]Department of Earth, Atmospheric and Planetary Sciences, Massachusetts Institute of Technology, Cambridge, MA 02139.

Abstract

Data from the Gravity Recovery and Interior Laboratory (GRAIL) mission have revealed that ~98% of the power of the gravity signal of the Moon at high spherical harmonic degrees correlates with the topography. The remaining 2% of the signal, which cannot be explained by topography, contains information about density variations within the crust. These high-degree Bouguer gravity anomalies are likely caused by small-scale (10's of km) shallow density variations. Here we use gravity inversions to model the small-scale three-dimensional

variations in the density of the lunar crust. Inversion results from three non-descript areas yield shallow density variations in the range of 100-200 kg/m^3. Three end-member scenarios of variations in porosity, intrusions into the crust, and variations in bulk crustal composition were tested as possible sources of the density variations. We find that the density anomalies can be caused entirely by changes in porosity. Characteristics of density anomalies in the South Pole-Aitken basin also support porosity as a primary source of these variations. Mafic intrusions into the crust could explain many, but not all of the anomalies. Additionally, variations in crustal composition revealed by spectral data could only explain a small fraction of the density anomalies. Nevertheless, all three sources of density variations likely contribute. Collectively, results from this study of GRAIL gravity data, combined with other studies of remote sensing data and lunar samples, show that the lunar crust exhibits variations in density by ±10% over scales ranging from centimeters to 100's of kilometers.

1. Introduction

Gravity analysis is an excellent tool for characterizing the nature of subsurface structures, since lateral density variations in the subsurface result in lateral variations in the gravity field. Gravity analyses have, for example, assisted in detecting faults, intrusions, changes in porosity or composition, variations in crustal thickness, and other structures beneath the surface (e.g., Andrews-Hanna et al., 2013; Soderblom et al., 2015; Milbury et al., 2015). High-resolution gravity data from the Gravity Recovery and Interior Laboratory (GRAIL) mission (Zuber et al., 2013a) provide constraints on the structure of the lunar crust at scales ranging from 10's to 1000's of km.

At long wavelengths, the gravity field largely reflects variations in the thickness and compensation state of the crust (Neumann et al., 1996; Wieczorek and Phillips, 1998; Wieczorek et al., 2013). It has been shown that ~98% of the power of the gravity signal at wavelengths less than ~68 km (spherical harmonic degrees greater than 80) is correlated with the topography (Zuber et al., 2013b). The remaining 2% of the signal cannot be explained by topography, and therefore contains important information about the subsurface. This subsurface signal is contained in the Bouguer gravity, which is the gravity field after it has been corrected for the effects of topography (Fig. 1). At half wavelengths greater than ~68 km, the correlation between topography and gravity is weak (Wieczorek et al., 2006) due to the effects of crustal thickness variations (Neumann et al., 1996; Wieczorek and Phillips, 1998; Namiki et al., 2009; Huang and Wieczorek, 2012; Wieczorek et al., 2013; Zuber et al., 2013b), mascon loading (Andrews-Hanna, 2013; Melosh et al., 2013; Freed et al., 2014), and lithospheric flexure. These long-wavelength signals are commonly inverted for global crustal thickness modeling, where the assumption is made that the crust of the Moon is characterized by either a constant density or by long-wavelength variations in regional density (Wieczorek et al., 2006; Wieczorek et al., 2013). However, downward continuation of the gravity anomalies to the crust-mantle interface causes a degree-dependent amplification, resulting in instabilities in the crustal thickness models at higher degrees. Recent GRAIL-derived crustal thickness models required a low-pass filter with an amplitude of 0.5 at degree 80 for global model stability (Wieczorek et al., 2013), despite the fact that there is negligible noise in the data even at much higher degrees (Zuber et al., 2013b). Therefore, the high-degree Bouguer anomalies cannot be entirely explained by variations in the thickness of the crust, and are instead likely dominated by small-scale (10’s of km) shallow density variations within the crust.

At small scales, most of the free-air gravity anomalies do correlate with topography, and provide a constraint on the mean density of the crust. Wieczorek et al. (2013) found that the lunar crust has an average bulk density of 2550 kg/m^3 and, assuming that the surface composition of the Moon is representative of the upper lunar crust, an average porosity of 12% down to depths of several kilometers. Regional density variations of ±250 kg/m^3 as revealed by the spectral correlation between gravity and topography can be explained by a combination of variations in composition and porosity (Huang and Wieczorek, 2012; Wieczorek et al., 2013). Subsequent studies have shown that the density also increases with depth in the crust outside the maria (Han et al.; 2014 Besserer et al., 2014), and is at least partially attributed to decreasing porosity with increasing lithostatic pressure and temperature. Both studies also found evidence for substantial lateral density variations at scales of 100's to 1000's of km with amplitudes of ±250 kg/m^3.

Gravity data have also been used to study small structures such as dikes, intrusions, and basin-related structures using forward models in the spatial domain (Andrews-Hanna et al., 2013; Kattoum and Andrews-Hanna, 2013; Kiefer, 2013). However, such analyses of GRAIL data must deal with the pervasive small-scale variability in the Bouguer gravity field that does not show any apparent correlation with known surface or subsurface structures. This variability is most apparent in maps of the Bouguer gravity gradients (Andrews-Hanna et al., 2013), in which the background variability is in many places comparable magnitude to signals arising from basin rings and giant intrusions into the crust. This variability can in some cases be circumvented by averaging along lines of symmetry, such as azimuthal averaging around basins (Andrews-Hanna, 2013; Kattoum and Andrews-Hanna, 2013), linear averaging parallel to dikes (Andrews-Hanna et al., 2013), or area-weighted averaging across impact craters (Soderblom et al., 2015).

Thus, both spherical harmonic crustal thickness modeling and spatial domain studies of discrete structures are limited by the substantial small-scale variability in the lunar gravity field. This variability can be minimized by appropriate filtering and averaging, effectively treating it as noise. However, the power and error spectra of the gravity clearly show that this background variability is not noise (Zuber et al., 2013b). Rather, this variability should be considered to be a geologic signature that contains real and important signal due to small variations arising from the natural complexity of the crust (Fig. 2A). These short-wavelength Bouguer signals typically cannot be attributed to either any surface structure or to relief along the crust-mantle interface, and must therefore be interpreted as arising from subsurface density variations within the crust. For crustal thickness modeling, the large scale signal is mainly of importance and so a filter is applied to the Bouguer gravity in the spectral domain that removes these short wavelengths (Fig. 2A, black line). In order to enhance the small-scale features, the inverse of that filter can be applied, capturing all anomalies not associated with crustal thickness variations (Fig. 2B, red line).

From remote sensing we know that the lunar crust is composed mainly of anorthosite, formed as a floatation crust from the lunar magma ocean (Smith et al., 1970; Wood et al., 1970); Warren and Wasson, 1977, 1979; Warren, 1985. However, the samples obtained from the Apollo missions, as well as lunar meteorites, show that the lunar crust is compositionally heterogeneous, with major rock types including anorthosite, norite, troctolite, and sometimes gabbro (Dymek et al., 1976; Papike et al., 1998; Warren, 1993; Wieczorek et al., 2006). The samples vary widely in both porosity and density (Kiefer et al., 2012a), and the distribution of equivalent rocks in the crust is not constrained. Similar variations in density arising from composition and porosity would be the likely explanation for both the large-scale and small-scale

density variations observed in the GRAIL data. Thus, the crustal density is variable on all length scales, from 100's to 1000's of km as revealed by the correlation between gravity and topography (Wieczorek et al., 2013), down to 10's to 100's of km as revealed by the small-scale Bouguer anomalies, even down to the scale of centimeters as revealed by lunar samples (Kiefer et al., 2012a).

The goal of this study is to investigate the nature and source of the small-scale variability in the gravity field revealed by GRAIL. We use continuous density inversions (Li and Oldenburg, 1996; 1998; Liang et al., 2014) to model small-scale density variations in the lunar crust. We first test the model by applying it to the mantle uplift beneath the Freundlich-Sharonov impact basin. Next we compare our model results to previous work done on narrow linear features found in the gravity gradients of the GRAIL data (Andrews-Hanna et al., 2013). Then we use synthetic data in order to investigate the sensitivity of the model results. Next, we invert the gravity of small areas on the Moon that lack clear large-scale features such as impact basins large enough (≥200 km in diameter) to exhibit mantle uplift that would dominate the gravity anomalies (Neumann et al., 2015; Milbury et al., 2015). Finally, we use the derived density model to test possible interpretations of these small-scale density variations, using constraints from lunar samples, remote sensing data, and other sources of information.

2. Methods

2.1. Inversion

Bouguer gravity anomalies arise from variations in bulk density in the subsurface. These variations can be characterized by the spatially varying density anomalies $\rho(x, y, z)$, and they produce an anomalous gravity field, $\vec{g}_s$, that adds to the ambient gravity field. Using

GRAIL data, we calculate the vertical component of this anomalous gravity field, g_z, which relates to the anomalous density distribution. If one considers the anomalous gravity and density locally in a Cartesian coordinate system, the relationship is given by:

$$g_z(\vec{r}_0) = G \int_V \rho(\vec{r}) \frac{z - z_0}{|\vec{r} - \vec{r}_0|^3} dv \tag{1}$$

where G is the gravitational constant, V represents the volume of the density model, $\vec{r}_0$ is the vector indicating the location of the observation point, $\vec{r}$ is the location of a source volume element dv, z_0 is the vertical position of the observation point, and z is the vertical position of the source volume element. For each volume element in a three-dimensional density contrast model, we calculate the resulting vertical component of the gravitational acceleration acting on each point in a two-dimensional observational grid.

Equation 1 can be evaluated by discretizing the three-dimensional density distribution into model cells of unknown density anomaly. The gravity anomaly arising from the jth cell at the ith observation point can then be written as:

$$\begin{aligned} g_z(\vec{r}_0) &= \sum_{j=1}^{M} \rho_j \left\{ G \int_{\Delta V_j} \frac{z - z_0}{|\vec{r} - \vec{r}_0|^3} dv \right\} \\ &\equiv \sum_{j=1}^{M} \rho_j A_{ij} \end{aligned} \tag{2}$$

where ρ_j and ΔV_j are the density contrast and volume of the jth cell, respectively. The parameter A_{ij} is a matrix that quantifies the contribution of the jth cell to the ith datum, and M is the total number of model cells. In matrix notation this equation becomes:

$$\vec{g} = \boldsymbol{A}\vec{\rho} \tag{3}$$

where $\vec{g}$ is a vector representing the anomalous gravity data, and $\vec{\rho}$ is the vector containing the density contrast values of the M cells. One approach to gravity interpretation is to find the density contrast distribution that satisfies Eq. 3. However, the solution for a three-dimensional density distribution will be non-unique. Furthermore, any noise in the data will introduce errors into the inverse solution, further reducing the reliability of the model.

The inversion minimizes the residual vector within reasonable limits based on the expected noise in the data. One commonly used method is regularized inversion. We use the algorithm by Li and Oldenburg (1996, 1998), in which the inverse problem is formulated as an optimization problem where an objective function of the density model is minimized. The objective function is given by:

$$\phi = \phi_d + \beta\phi_m \tag{4}$$

where ϕ_d is a measure of the data misfit, ϕ_m is the model objective function that measures the smoothness of the model, and β is a regularization parameter. The goal is to construct a model that fits the data, but that is also characterized by smooth variations in density. Due to the non-unique nature of the problem, there are an infinite number of possible solutions, but those

solutions with smoothly varying density anomalies are simpler and therefore preferred. This tradeoff between model smoothness and data misfit is controlled by the regularization parameter β. The function for the model norm used in GRAV3D (Li and Oldenburg, 1996, 1998) is:

$$\phi_m(\rho) = \alpha_s \int_V \{w^2(z)(\rho - \rho_0)^2\} dv + \alpha_x \int_V \left\{\left(\frac{\partial(w(z)(\rho - \rho_0))}{\partial x}\right)^2\right\} dv$$
$$+ \alpha_y \int_V \left\{\left(\frac{\partial(w(z)(\rho - \rho_0))}{\partial y}\right)^2\right\} dv \qquad (5)$$
$$+ \alpha_z \int_V \left\{\left(\frac{\partial(w(z)(\rho - \rho_0))}{\partial z}\right)^2\right\} dv$$

where ρ is dependent on x, y, and z, ρ_0 is the mean density contrast which in this case is assumed to be zero as there is no assumed density structure, α_s, α_x, α_y, and α_z are weighting factors that affect the relative importance of the different components of the objective function i.e. how important is model smoothness in any specific direction or overall. These terms can be adjusted based on some *a priori* expectations of the resulting density model. We have no *a priori* information to justify different choices for α_x, α_y, and α_z, and thus set them equal to one another. The ratio of α_x to α_s must scale with dx^2, where dx is the model cell size. Testing of this inversion model during its development (Li and Oldenburg, 1998) led to a preferred choice of $\alpha_x = 4\ \alpha_s \cdot dx^2$, and we adopt this weighting in our analyses. The effect of choosing a different scaling between the α parameters is discussed in Section 4.1. The $w(z)$ term in equation (5) is a depth weighting function, used to counteract the decay of the gravity with depth:

$$w(z) = (z + z_0)^{-1} \tag{6}$$

where z is the depth of the model point below the surface and z_0 is the height of the observational reference surface above the surface. The exponent of -1 is appropriate for point-source and small-scale gravity anomalies in order to counteract the decay of the gravity signal with distance (see Li and Oldenburg 1996, 1998). This depth weighting function encourages a more uniform distribution of density anomalies with depth, rather than their concentration at the surface. The data misfit is represented using a 2-norm measure (Li and Oldenburg, 1996, 1998):

$$\phi_d = \left\| W_d \left(\vec{g}_{pre} - \vec{g}_{obs} \right) \right\|^2 \tag{7}$$

where $\vec{g}_{pre}$ is the predicted gravity data from the model density solution, and $\vec{g}_{obs}$ is the measured 2D gravity anomaly, and W_d is a data weighting diagonal matrix whose diagonal elements are $1/\sigma_i$ in which σ_i is the standard deviation of the ith datum.

We use the spherical harmonic GRAIL gravity model GRGM900B_BOUGUER (Zuber et al., 2013b; Lemoine et al., 2014) without the degree-0 term, where a uniform crustal bulk density of 2550 kg/m^3 (Wieczorek et al., 2013) was used to calculate the Bouguer gravity anomaly field. The gravity inversions assume a flat Cartesian coordinate system, but the effects of this flat geometry rather than the true spherical shape of the Moon on the resulting density anomalies should be at the ~2% level, and have no impact on our conclusions. The corresponding free-air gravity field has a signal to noise ratio that ranges from ~65,000 to 15 for degrees 80 to 550 based on the power and error spectra. Given that only ~2% of the signal arises from the subsurface, the Bouguer signal to noise ratio is reduced to ~1300 to 0.3 over the range

of degrees of interest. Although this indicates that a non-trivial amount of noise is included in the data being inverted, the inversion algorithm is designed to accommodate this noise. For the gravity field used in our solution (GRGM900B_BOUGUER) no Kaula constraint was applied at degrees lower than 600. This implies that at the lower degrees the Ka Band Range Rate data completely determine the spherical harmonics coefficients. To characterize the spatial variations of the error in the data, we use clone fields (that can be obtained from: http://pds-geosciences.wustl.edu/grail/grail-l-lgrs-5-rdr-v1/grail_1001/extras/clones/), which are different solutions of the spherical harmonic coefficients that describe the data equally well within one standard deviation of the best-fit field. We use 50 statistically equivalent clone fields to calculate the error σ_i at each datum.

The regularization parameter, β, is varied so as to optimize the tradeoff between ϕ_d and ϕ_m. The model is run for a range of β values, and the resulting model norm (ϕ_m) is plotted against the data misfit (ϕ_d). This plot is called a Tikhonov curve, or L-curve (Hansen, 1992) due to its typical L-shape, and the optimal β is chosen at the elbow of the curve. The model predictions are sensitive to the chosen value of β, and the difference in predicted density anomalies over an order of magnitude in β can be around 40%. For the smallest values of β considered, the models predicted unphysically large and small densities; whereas for the largest values of β considered, the modeled density anomalies are overly smooth and do not adequately fit the gravity data.

2.2. Analysis of the Inversion Results

Given a model of the density variations within the crust, the next step is to test different interpretations of the source of those density anomalies against that model. Lunar samples

exhibit a range in both composition and porosity that collectively contribute to differences in density (Dymek et al., 1976; Warren, 1993;Papike et al., 1998; Wieczorek et al., 2006; Kiefer et al., 2012a). While it is not possible to break this degeneracy between composition and porosity with gravity data alone, by testing end-member scenarios, we can evaluate which sources of density variations may have the dominant contribution to the background variability. Here, three end member scenarios are considered as possible causes of the variations in bulk density: variations in porosity, in the fractional volume of high-density volcanic intrusions, and in the composition of the primary crust itself. In reality, a combination of these scenarios likely contributes to the observed gravity field.

In evaluating the model predictions, we must consider the nature of the inversion results, which allow for long tails in the distribution of density anomalies at both high and low values. In any model, a small subset of points may exceed most reasonable constraints based on our end-member scenarios. Furthermore, orbital data tend to smooth out the smallest scales of variability, while the limited number of Apollo samples which have been analyzed (Kiefer et al., 2012a) may not capture the full range of possible properties. Rather than exclude any of our end-member scenarios based on outliers from the inversions, we conservatively compare either the plus or minus one standard deviation ($\pm 1\sigma$) range in model predictions of the top 20 km of the density model solution with observational constraints, or compare $\pm 2\sigma$ value with the minimum or maximum allowable value (e.g., the compositional fraction of noritic anorthosite or intrusions in the crust cannot be less than 0% or greater than 100%).

In the first end-member scenario, we assume that all variations in density are purely due to changes in porosity (i.e., a change in bulk density). Variations in porosity are calculated by

adding the average regional bulk density (Wieczorek et al., 2013) for each region to the modeled density variations and calculating the porosity as follows:

$$\phi(x,y,z) = 1 - \frac{(\rho(x,y,z) + \bar{\rho})}{\rho_g} \tag{8}$$

where $\rho(x,y,z)$ is the recovered density contrast model, $\bar{\rho}$ is the average regional bulk density, and ρ_g is the grain density of typical lunar highland rock, which we assume to be 2900 kg/m^3 (Kiefer et al., 2012). The porosity measured for a subset of lunar samples ranges between 2% and 20% (Kiefer et al., 2012a), representing the porosity variations at the scale of individual rocks. Wieczorek et al. (2013) calculated variations in the crustal bulk density by minimizing the correlation coefficient between the Bouguer gravity and the topography in the spectral domain, with the majority of the crust exhibiting densities between 2300 and 2800 kg/m^3. The grain density was obtained from an empirical relationship between the grain density and FeO and TiO_2 concentrations, which was then used to calculate the porosity (Wieczorek et al., 2013). The range in porosity determined through this method of 4 – 21%, representing mean porosity variations in the top few kilometers, at horizontal spatial scales of 100's of km, is consistent with the observed porosity range obtained from the lunar samples. Given the similarity in the ranges in observed porosities at scales of 10's of cm and 100's of km, we expect that porosity variations at intermediate (10-km) scales should fall within a similar range. For a given region, we assume that a $\Delta\rho$ of 0 kg/m^3 from the inversion equates with the average porosity of the area (Wieczorek et al., 2013). The porosity end-member is then considered plausible if the model-predicted $\pm 1\sigma$ porosity range falls within the observed range of 2–21%.

The next end-member scenario considered the possibility that all variations in density are due solely to intrusions into the crust. Evidence for intrusions into the crust has been found in

different contexts. For example, any mare extrusion must have been emplaced through a dike or other conduit, and these solidified magma conduits likely remain today (Head and Wilson, 1992). Sills are inferred beneath floor-fractured craters, and similar intrusions could conceivably exist even in craters lacking fractures as well as in the surrounding crust (Jozwiak et al., 2012, 2015). Cryptomaria are a form of hidden extrusive eruption that may contribute to the gravity on a range of scales (Whitten and Head, 2013; Whitten and Head, 2015a, 2015b; Sori et al., 2016). Plutons inferred to be the source of Mg-suite like intrusions may contribute to the density anomalies in the crust (Prissel et al., 2014). Intrusions are also inferred beneath linear rilles (Head and Wilson, 1993) and associated with linear gravity anomalies (Andrews-Hanna et al., 2013). Remote sensing signatures that are typical for the highlands indicate the possibility of some mafic material mixed into the crust (Hawke, 2003; Prettyman et al., 2006; Ohtake et al., 2009; Pieters et al., 2009; Cheek et al., 2013; Crites and Lucey., 2015) . Outcrops of pure anorthosite are rare, and generally arise from deeper crustal levels (Warren, 1990; Hawke at el., 2003; Longhi, 2003; Ohtake et al., 2009; Cheek et al., 2013).

For this end-member scenario, we assume that the model density 2σ below the mean predicted by the model, equates with intrusion-free crust with the average crustal density of the specific area (Wieczorek et al., 2013), and increases in density are due to the presence of intrusions. The 2σ value was chosen as it contains most (95%) of the signal, but excludes any outliers as discussed above, though admittedly this choice is somewhat arbitrary. Since the model density distribution is inherently smooth and the model cell size (10x10x2 km) is larger than typical intrusions, we assume that each model cell is only partially composed of intrusions. We calculate the intrusion fraction in each cell from the density anomalies by assuming a density contrast of 600 kg/m^3 for intrusions, based on an intrusion bulk density of 3150 kg/m^3 (Kiefer et

al., 2012a), appropriate for a lunar gabbro, and the appropriate regional crustal density at the locations of interest of 2550-2600 kg/m^3 (Wieczorek et al., 2013). The amount of FeO derived from remote sensing studies yields a range of 15%-45% of intrusive materials in typical highland terrain, under the assumption that the fraction of material in the regolith is representative of the fraction of intrusions at depth (Crites and Lucey, 2015). This range represents the two end-member assumptions made, either pure intrusions due to post-magma ocean igneous activity, or material that originated in the mantle. Floor-fractured craters (Jozwiak et al., 2012, 2015, 2016; Thorey et al., 2015) and other structures also provide evidence for shallow magmatic intrusions and sill formation, though they do not provide specific constraints on the fractional volume of intrusives in the lunar crust more generally. This end-member interpretation is tested against the model results by assuming that the modeled mean $+2\sigma$ fraction range of intrusive material should not exceed 100%, but with the preferred result that the modeled mean $+1\sigma$ fraction of intrusive material should not exceed the expected range obtained from remote sensing (Crites and Lucey, 2015) of 45%. This approach is conservative in that the GRAIL-derived densities are most sensitive to the upper several kilometers, whereas density is expected to increase with depth (Besserer et al., 2014), which would reduce the density contrast between the crust and the intrusions. For a given allowable range for the fraction of intrusive material, the increase in density with depth would place a stricter constraint on the allowable model density contrasts due to intrusions alone.

Remote sensing data indicate that the bulk of the lunar highlands surface is composed of a mixed feldspathic layer of a few 10's of km thick, likely composed of a mixture of ferroan anorthosite, anorthositic norite, and noritic anorthosite (Cheek et al., 2013; Hawke, 2003). In the previous scenario, such a composition was interpreted as representing intermixed primary crust

and intrusive material, but it may also arise from compositional variations (and the FeO content in particular) of the primary crust itself. In the previous end-member scenario, we assume that the predicted variations in density are due to compositional variations between pure anorthosite, and anorthositic norite or noritic anorthosite, each of which is represented in the lunar samples (Kiefer et al., 2012a). Assuming that the -2σ density in the inversion solution corresponds to pure anorthosite, which has a grain density between 2710-2750 kg/m^3 (Kiefer et al., 2012a; 2012b), and any increase in grain density is due to an increased fractional content of anorthositic norite or noritic anorthosite, which have similar grain densities, in the range of 2840-2910 kg/m^3 (Kiefer et al., 2012a), the maximum density contrast expected for this end-member scenario is ~200 kg/m^3. The predicted density anomalies are used to calculate the fractional abundance of anorthositic norite relative to an anorthosite background (with pure anorthosite defined as the -2σ model density, and with the constraint that the mean $+2\sigma$ anorthositic norite fraction from the model cannot exceed 100%).

3. Model tests

This inversion model has been extensively benchmarked in previous studies, including the inversion of forward-modeled gravity from synthetic subsurface density anomalies in simple geometric shapes (a cube), and more complex shapes (step-like density anomalies). Li and Oldenburg (1998) found in their synthetic examples that the inversion method recovers the general shape and depth accurately. However the recovered model is smoother and therefore has a lower amplitude (90% in the center and 60% at the edges) than the original model. Here, we perform additional tests more specific to the Moon and the small-scale density variations of interest in this work.

3.1. Freundlich-Sharonov

We first applied the model to the Freundlich-Sharonov basin on the farside of the Moon (Fig. 3) in order to test the model against a large-scale Bouguer anomaly arising from deep mantle uplift that is well-resolved Moho uplift models. A recent study used a similar continuous density inversion to obtain a global model for density variations, including all spherical harmonic degrees (Liang et al., 2014). That study showed that the predicted density anomalies beneath the lunar basins are consistent with the expected density anomalies arising from an uplifted mantle plug. Another study showed that mantle uplift dominates the gravity signal for a crater diameter larger than ~200 km (Milbury et al., 2015). We performed a similar local analysis of Freundlich-Sharonov as a test of our model. For this model we do not apply a high-pass filter to the Bouguer gravity data, as we are interested in the long-wavelength structure of the basin. The Bouguer gravity (Fig. 3A) shows a strong positive anomaly in the basin center corresponding to the uplifted mantle plug (Neumann et al., 1996; Wieczorek and Phillips, 1998; Wieczorek et al., 2013; Melosh et al., 2013; Freed et al., 2014).

We performed the inversion for a range of β values, and find the optimal model for a β of 10^{-2} using the elbow point, or maximum curvature, of the L-curve (Fig. 3B). For this example, the L-curve spans a very short range in model smoothness (φ_m), while the range in data misfit (φ_d) spans several orders of magnitude. Due to the the large size and magnitude of this anomaly, the model norm is dominated by the range in density rather than the density gradient, and fitting the data more closely has little effect on the model norm. The resulting density model shows a strong positive density anomaly beneath the basin that is consistent with the expected central uplift of mantle material (Fig. 3C). For comparison to the density model, the crustal thickness was modeled (Fig. 3D) using the software package SHTOOLS (Wieczorek, 2014), assuming an

average crustal density of 2550 kg/m^3, an average mantle density of 3150 kg/m^3, and a mean crustal thickness of 40 km, reproducing the model of Wieczorek et al. (2013). The shape and location of the positive density anomaly from the continuous density inversion is consistent with the crustal thickness model. The inversion solution puts most of the density contrast at depth, as expected for uplifted mantle, showing that the depth weighting function behaves as expected for large, deep anomalies. The predicted density contrast of ~600 kg/m^3 is consistent with an average crustal density of 2550 kg/m^3 and a mantle density of 3150 kg/m^3 (Wieczorek et al., 2013). The density anomaly extends from the base of the model domain up to ~16 km depth, based on the average depth beneath the basin at which the density anomaly is at 50% of its maximum value, which is consistent with the expected depth of the crust-mantle interface obtained from crustal thickness modeling. These results are also consistent with the global continuous density inversions of the GRAIL data (Liang et al., 2014), indicating that the Cartesian geometry assumed in this study (rather than the global spherical inversion of Liang et al. (2014) is adequate for local studies.

3.2. Giant dike-like structures

We tested the sensitivity of the model against the results of a study of small-scale gravity anomalies originating in the shallow subsurface: long, linear gravity anomalies, interpreted to be giant dike-like intrusions (Andrews-Hanna et al., 2013). Here we examine one of these features in the northern farside highlands (centered at 68°N, 169°E) in more detail.

The unfiltered Bouguer gravity reveals a linear positive gravity anomaly as expected based on the gravity gradients (Fig. 4A). We perform the inversion for a range of β values, and again find an optimal objective function β of 10^{-2} (Fig. 4B). Compared to the L-curve of the

Freundlich-Sharanov Basin, the linear gravity anomaly has a broader range in model smoothness (φ_m). The inversion result shows a narrow feature with a positive density contrast of ~300 kg/m^3 that extends to a depth of ~25-30 km, and has an average width of about 18-24 km (Fig. 4C&D). Both the dimensions and the density contrast are consistent with the results from Andrews-Hanna et al. (2013), though our continuous inversion predicts a broader, shallower, smoothly varying density distribution. We attribute the differences to the fact that Andrews-Hanna et al. (2013) fit the gravity using a single, discrete density anomaly, which requires the feature be buried more deeply in order to match the width and smoothness of the observed gravity anomaly. While the discrete density anomaly is likely a better explanation for the linear gravity anomalies, a smooth and continuous density distribution likely provides a better explanation for the pervasive small-scale, and seemingly random gravity anomalies that are the subject of this study. These two tests show that the model is sensitive to, and accurately recovers, density anomalies located anywhere from the near surface, to the crust-mantle interface.

3.3. Synthetic models

Next, we use synthetic models to test scenarios representing continuous, smoothly varying density variations. For the first test we use a random Gaussian generator to simulate density variations with a 1-σ amplitude of 300 kg/m^3, which are similar in shape and magnitude to the observed density variations discussed in the next section. We use a forward-model to calculate the gravity ($\vec{g}_z$) that would result from the synthetic density model. A 2% Gaussian noise field ($\vec{\varepsilon}$) is added to the resulting gravity field, simulating background noise in the data (exceeding the noise in the GRAIL data over most degrees (Zuber et al., 2013b; Konopliv et al., 2014)). We invert the resulting gravity field, as described above, and compare the resulting

density model to the input synthetic density model. The optimal model recovers the shape of the density variations well within the top ~20 km, but is substantially lower in amplitude, as it only recovers ~60% of the original signal (Fig. 5).

This test demonstrates that, for random continuous density distributions, the model correctly reproduces the distribution of anomalies in the upper crust but underestimates their magnitude. The lack in recovery of deeper sources is likely due to the fact that gravity decays as $1/r^2$, where r is the distance between the observer and the anomaly, and the attenuated anomalies from these deeper sources are overwhelmed by the anomalies arising from shallower depths. This imperfect recovery at depth is not an artifact of the depth weighting function, used in the inversion modeling, because the Freundlich-Sharanov model test in section 3.1 shows that the inversion method does put large anomalies at depth. For isotropic density anomalies, the gravity is only sensitive to anomalies at depths less than or comparable to the wavelength of density variation (~20 km at degree 550). The example case of the Freundlich-Sharonov Basin shows us that at greater amplitudes and longer wavelengths, the density signature can also be detected at greater depths. However, these amplitudes and wavelengths are not reached for the small-scale density anomalies that we are considering in this work. The loss of amplitude of the shallow anomalies may be due to vertically superimposed, or laterally adjacent, anomalies of opposing sign partially cancelling one another. This can be seen in the model results where large magnitude density anomalies arising at depths greater than ~20 km were modeled as lower magnitude anomalies at shallower depths. Some loss in amplitude may also arise from the smoothing of small-scale anomalies by the inversion. In evaluating the inversion results from the small-scale gravity anomalies in the next section, the recovery of signals only in the top 20 km, and the loss in amplitude of these near-surface anomalies, must be taken into consideration.

4. Small-scale density anomalies

4.1. Small-scale density anomalies in non-descript areas of the crust

In the previous sections, distinctive structures in the subsurface were analyzed to demonstrate that the continuous density inversion gives results that, while non-unique, are both physically reasonable and consistent with expectations based on previous studies. In this section, we use GRAIL data to examine the nature and origin of the pervasive small-scale gravity anomalies that do not appear to be associated with particular structures. The Bouguer gravity is dominated by impact basins (Fig. 1B; Neumann et al., 2015). However, the aim of this study to model and determine the source of the small-scale gravity anomalies observed everywhere in the data. For this reason we investigate regions that are distant from known impact basins. Even away from impact basins, the long-wavelength Bouguer anomalies are thought to be associated with variations in crustal thickness (Wieczorek et al., 2013). To isolate the signal from these long-wavelength anomalies, we apply a high pass filter to the data. As discussed previously, GRAIL-derived crustal thickness models require substantial filtering to avoid instabilities arising from the amplification of short-wavelength gravity anomalies during downward continuation to the crust-mantle interface. These high-degree anomalies must originate at shallower depths than the crust-mantle interface. The GRAIL crustal thickness models were calculated using a minimum amplitude filter (Wieczorek and Phillips, 1998), which is a smoothly varying low-pass taper (Fig. 2B, black line) with an amplitude of 0.5 at degree 80 for the GRAIL crustal thickness models (Wieczorek et al., 2013).

Under the assumption that all of the gravity signal results either from variations in crustal thickness or from density anomalies within the crust, it can be assumed that the portion of the signal not used for crustal thickness modeling is the result of the small-scale density

variations. Therefore, we define a high-pass filter equal to one minus the minimum amplitude filter (the "complementary minimum amplitude filter"; Fig. 2B, red line), which uses those spectral components of the Bouguer gravity that is not being used for crustal thickness modeling. The complementarity is only approximate, as the minimum amplitude filter is applied to the relief along the crust-mantle interface rather than the Bouguer anomaly itself. There is no unique filter to isolate signals arising within the crust, just as there is no unique filter to isolate signals arising from the crust-mantle interface. However, for globally stable models of crustal thickness and crustal density anomalies, some pair of filters resembling the minimum amplitude filter used by Wieczorek et al. (2013), and the complementary minimum amplitude filter used here, is required. Although it is possible to attribute Bouguer gravity anomalies of all wavelengths to continuous subsurface density variations (e.g., Liang et al., 2014), it is not possible to attribute anomalies of all wavelengths to variations in relief of along the crust-mantle interface. Since our focus is on the small-scale density variations in the crust that cannot be ascribed to relief along the crust-mantle interface, our results are not sensitive to the choice of filter, provided that it is complementary to a stable crustal thickness model. Different types of filter have also been considered, such as a cosine taper, and though the results vary slightly, the overall conclusions are not sensitive to the chosen type of filter. We also apply a low-pass cosine taper from degree 550 to 600, where noise begins to dominate the signal (Zuber et al., 2013a). Although other filters could be designed, the density inversions in this section provide a set of models that, together with the GRAIL crustal thickness model (Wieczorek et al., 2013), can account for all the signal in the gravity data.

A spatial map of the GRAIL gravity model GRGM900B_BOUGUER (Zuber et al., 2013b; Lemoine et al., 2014) was created using the complementary minimum amplitude filter

(Fig. 1B). Three areas were chosen for study (Figs. 1, 6, 7, 8, 9) because they lack large impact basins that would be expected to exhibit prominent mantle uplift (Wieczorek et al., 2013; Neumann et al., 2015) and to contain solidified impact melt pools (Vaughan et al., 2013; Spudis et al., 2014). The filtered Bouguer gravity maps of these areas are similar in character, with substantial variability but no clear discrete structures. Regions that are 150 km to 400 km in size were isolated from the gravity data at a horizontal resolution of 5 km per pixel, centered on 32°S, 57°E (area 1, Fig. 7), 19°N, 220°E (area 2, Fig. 8), and 0°N, 122°E (area 3, Fig. 9).

A typical L-curve for the inversion models show that the optimal β is very similar to that found in the examples in section 3 (Fig. 10). Though L-shape of this curve is not as pronounced as in the other cases, the optimal β was chosen by finding the maximum second derivative. The best-fit solutions from the inversions yield density anomalies that are similar in magnitude at all three areas (Figs. 7, 8, and 9), with a typical range of approximately ±100-200 kg/m^3. The inversion results also show that density variations are only predicted in the top ~20 km of the crust. However, as discussed above, this is an expected result for a random, continuous variation in density due to the attenuation of gravity with distance, such that deeper small-scale anomalies are masked by the near-surface anomalies and are not resolved in the model. Therefore, we only consider the results in the upper 20 km of the model.

We next test the three end-member scenarios for the sources of the density anomalies. As discussed above, lunar samples exhibit a porosity range of 2-20% (Kiefer et al., 2012a). The inversion results predict 1σ ranges in porosity from 8%-19% (Table 1) varying around the mean porosity obtained from Wieczorek et al. (2013), which is consistent with the range observed in the lunar samples. Thus, the end-member scenario in which the majority of density anomalies

arise from variations in porosity is a possible explanation for the small-scale density variations in these non-descript areas.

The second end-member scenario considered is that the majority of variations in density are due to intrusions into the crust. For areas 2 and 3, we calculate a fractional volume of intrusions with a 1σ range of 8%-50% (Table 1). We assume a lunar gabbro intrusion with a bulk density of 3150 kg/m^3 (Kiefer et al., 2012a). The predicted fractions somewhat exceed the expected $\pm 1\sigma$ range of 15%-45% (Crites and Lucey, 2015) and the $+2\sigma$ fraction of 67% is below the upper bound of 100% (values above which are physically impossible). Area 1 however, has a calculated fractional volume of intrusions with a 1σ range of 36%-110%. This is outside the expected range, and the $+2\sigma$ fraction is 148% (physically impossible). Therefore intrusions could also explain the majority of the small-scale density variations for areas 2 and 3, but this explanation is unlikely for area 1.

For the third end-member scenario, we assume that the majority of the variations in density in the subsurface are due to compositional variations between ferroan anorthosite and anorthositic norite or noritic anorthosite. The Moon may have a two-layered crust, consisting of an upper pure anorthosite crust and a lower noritic crust (Wieczorek et al., 2006). If this is the case, reworking of the crust by impactors may have mixed these two layers creating a compositional and density variations that we can detect with GRAIL data. Differences between pure anorthosite and anorthositic norite yields a density contrast of about 200 kg/m^3 (Kiefer et al., 2012a). We calculate a fractional volume of anorthositic norite or noritic anorthosite with $\pm 2\sigma$ ranges between 0% and 98% for area 3, but with +2σ values of 290% and 180% for areas 1 and 2, respectively (Table 1). The $\pm 2\sigma$ values for area 3 is close to 100%, which implies that the majority of the observed density contrast can be explained by changes in bulk crustal

composition. However, areas 1 and 2 require fractional volumes of anorthositic norite much greater than 100%, which implies that the majority of the density contrast cannot be explained by changes in crustal composition alone.

These analyses, however, assume that the inversion accurately retrieved the magnitude of the density anomalies. The forward model we describe in section 3.3 suggests that the inversions only recover 60% of the magnitude of the anomalies. Therefore, we repeat the end-member scenario calculations, but with an increase in amplitude in the modeled density (Table 2). For the first end-member scenario, in which changes in density are mainly due to porosity, we calculate a porosity range of 9%-21%. The calculated porosity is still within the accepted limits, and so the majority of the density variations can be explained by changes in porosity. For the second end-member scenario, where changes in density are due to compositional variations between pure anorthosite and noritic anorthosite or anorthositic norite, the $\pm 2\sigma$ value for all three areas greatly exceeds 100%. Area 3 has a fractional volume of noritic anorthosite with a mean $\pm 1\sigma$ range of 41%-123%, and areas 1 and 2 have a range of 46%-367%. The 1σ range for areas 1 and 2 greatly exceed 100%, so this end-member scenario alone cannot explain the majority of observed density variations. For the last end-member scenario, where the density variations are due to intrusions into the crust, the $\pm 1\sigma$ range for area 3 of 14%-41% is in the expected range of 15%-45% (Crites and Lucey, 2015), while the range for areas 1 and 2 of 58%-183% and 29%-85%, respectively, greatly exceed the expected range. These results indicate that this end-member scenario can explain the majority of modeled density variations for area 3, but can only explain a fraction of the modeled density variations for areas 1 and 2.

These results indicate that porosity variations can explain the majority of the observed density variations in all three areas, while intrusions can explain the majority of the density

variations in area 3 and possibly area 2. Compositional variations of the bulk lunar crust are unlikely to explain the majority of the density variations in any area once the imperfect recovery of the magnitude of the density anomalies is taken into account. From sample data and remote sensing observations we know that the crust varies in both composition and porosity, therefore, the most likely explanation for the density variations is a combination of the three end-member scenarios. The results of our end-member calculations, however, suggest that porosity variations likely play the dominant role.

As previously noted in section 2.1, the model results are sensitive to choice of β. We have chosen the optimal model in this work based on a tradeoff between model smoothness and fit to the data, but we cannot rule out other models. Taking area 1 as an example, the 1σ range in density for the optimal model (β=10^{-3}) is 110.5 kg/m^2. An increase in β by an order of magnitude results in a 1σ range of 71.9 kg/m^2 (a decrease in density range of 35%). This higher β value would similarly decrease the required ranges in porosity, crustal composition, and intrusion fraction. A decrease in β by an order of magnitude yields a 1σ density range of 188.6 kg/m^2 (an increase in density range of 41%). This lower β value would increase the required ranges in porosity, crustal composition, and intrusion fraction. However, the models that have a higher β are overly smooth, lack detail, and provide poor fits to the data, effectively not taking advantage of the extraordinarily high resolution of the GRAIL data. The models that have a lower β show a great deal of detail but loose coherency and require unrealistically large variations in density, and therefore are not geologically likely. Nevertheless, the range in porosity can be stretched to beyond what is observed in lunar samples by choosing a smaller β, or the range in predicted fractional volume basalt and compositional variations can be reduced so as to allow these end-members to explain all the density variations by choosing a larger β. The inversion is also sensitive

to the relative weighting of the different terms in ϕ_m (α_s in comparison to α_x, α_y, and α_z). If we increase or decrease α_s by an order of magnitude relative to α_x, the magnitude of the resulting density anomalies decrease or increase by approximately 40%, respectively. Although our results from the optimal value of β and the nominal values for the weighting of the terms in the objective function are our preferred results, we cannot rule out density anomalies ~40% larger or smaller. Therefore it is important to perform additional analyses to test the consistency of the inversion results, which we do in the next sections using analyses of the floors of impact basins and comparison of the models to remote sensing data.

4.2. Basin floors

To investigate the timing and nature of the emplacement of the small-scale density anomalies, we turn our attention to the floors of large basins. If the formation of these small-scale gravity and density anomalies predates the formation of a basin, we should expect to see no evidence for such anomalies in the floor of the basin, since pre-existing density anomalies of any sort would be expected to be homogenized in the impact melt pool. If, however, the formation of the small-scale density variations is a constant process that continued beyond the formation of the major basins, smaller amplitude anomalies would be expected.

Two basins are analyzed: Imbrium basin and South Pole-Aitken basin (hereafter referred to as SP-A). The gravity gradients within the Imbrium basin are nearly uniform (Fig. 1), suggesting a lack of small-scale variability. This could potentially represent a basin that postdates the formation of the small-scale density anomalies found elsewhere in the crust. However, the inner depression within 195 km of the basin center has been filled with mare up to ~8-9 km in thickness (Solomon and Head, 1980), though later estimates put the mare thickness between 1.5 and 7 km (Gong et al., 2016). The low amplitude of anomalies in the gravity

gradients suggests that this basin fill is nearly uniform in density, as might be expected for volcanic fill, and indicates that the density variability seen elsewhere in the crust is not due to late stage (post-mare) generation of porosity variations. Gravity gradients decrease in amplitude proportional to the cube of the distance between the observer and the source, and thus the 2-9 km of mare fill would greatly diminish the amplitude of the gravity gradients at the surface arising from density anomalies beneath the mare.

In order to examine the small-scale density anomalies in the feldspathic crust beneath Mare Imbrium, we calculate the Bouguer gravity at the base of the mare infill (assumed to be at either 2 or 9 km depth) in the spherical harmonic domain. To prevent amplification of noise in the form of orbit parallel striping in the data at this location, the gravity was expanded out to spherical harmonic degree 350. The gravity data were then inverted and the mean and standard deviation of the density was calculated (Table 3). If we assume the mare thickness to be ~2 km, the standard deviation is 16 kg/m^3, which is significantly smaller than that of the non-descript area 2 of 33 kg/m^3 with the same filter applied (hence the results for area 2 differ somewhat from the discussed results in section 4.1 for this area). This would imply less variability under the Imbrium Basin. However, if we assume a mare thickness of 9 km the standard deviation increases to 52 kg/m^3, which is significantly greater than that of non-descript area 2 of 33 kg/m^3. The larger variability for Imbrium in this case may be either an effect of burial of pre-existing topography by the mare, or an effect of small density variations in the mare that have been amplified by the downward continuation. Due to this large range in possible standard deviation values, we cannot for certain say whether the small-scale variations predate or postdate the Imbrium Basin formation. It is conceivable that the small-scale variations are a continuous process and would therefore both predate and postdate the formation of Imbrium.

The same filter and inversion was then applied to a small area inside the SPA basin, where no subsequent large craters or basins dominate the signal (Table 3). The resulting density anomalies are 13% greater than those in non-descript area 2 (37.5 and 33.3 kg/m^3, respectively). This implies that the formation of the small-scale density variations postdate the formation of the SP-A basin. Furthermore, the bulk density of the crust in SP-A (2800 kg/m^3) is larger than the average density of the lunar highlands (2550 kg/m^3; Wieczorek et al., 2013). If the small-scale density anomalies were mainly caused by either intrusions into the crust or locally greater concentrations of norite, the density anomalies relative to the mean crustal density within SP-A should be smaller than in the highlands, in conflict with the model results. If the small-scale density anomalies are mainly due to variations in porosity, the magnitude of the density anomalies in SP-A should be ~10% greater than those in the farside highlands, in agreement with the density model results. Some of the lateral variations in density in the SP-A Basin could also be caused by differentiation of the deep impact melt sea (Vaughan et al., 2013; Vaughan and Head, 2014), but these variations are expected to be of a larger scale than the small-scale density anomalies we are considering here. Thus, the results from SP-A support the hypothesis that the main cause of the small-scale density anomalies, at least within these regions of the Moon, is variations in porosity.

4.3. Remote sensing

An alternative approach to determine the degree to which compositional variability contributes to the small-scale density variations, is to compare our results with constraints placed on the surface composition from remote sensing data. Such a comparison is complicated by the fact that the density models are sensitive to the top ~20 km of crust with a vertical resolution of 2

km, while remote sensing is only sensitive to the top few microns of the crust. However, impact gardening of the surface will tend to mix the upper regolith layer (Cashore and Woronow, 1985), which would make remote sensing observations representative of deeper levels. Here we assume that the composition inferred from remote sensing is representative of the top layer of the density inversion model. We use plagioclase, olivine, pyroxene, and iron oxide maps derived from a radiative transfer analysis of 400,000 Clementine UVVIS spectra (Figs. 11 and 12; Lucey, 2004). From these maps, we generate a global map of the (olivine+pyroxene)/plagioclase ratio (Figs. 11 and 12). The (olivine+pyroxene)/plagioclase ratio is representative of density because the ratio of mafic material to plagioclase in the simple mineralogy on the Moon is proportional to grain density, as the mafic materials have a higher density than the crustal materials. The top layer of each density model was resampled at the resolution of the remote sensing data (4 pixels per degree) and then compared to the four different mineral maps as well as the mineral ratio map. We tested for a correlation between the density model and the different mineral abundances by calculating the R^2 value and p-value for a least squares linear fit between each pair (Figs. 11 and 12). The p-value is the probability that obtaining the result is equal to or more extreme than what is actually observed for a given null hypothesis (in this case, that the density is correlated to the mineral map). We adopt a 2-σ threshold of 0.05. The R^2 value indicates what fraction of the variance is explained by this trend.

We find p-values <0.05 for Area 2 (Fig. 11) for the iron oxide, plagioclase and mineral ratio data, but the R^2-values are very small (below 10^{-2}), suggesting that there is a significant correlation, but this correlation only explains a small portion of the variance in the data. The p-values obtained for Area 3 (Fig. 12) are all well above the threshold for all mineral maps considered with the exception of olivine. However, the R^2 value for olivine is again very small

(below 10^{-2}), so here we can also conclude that compositional variations can explain only a very small fraction of the observed density anomalies. These results reveal that, at least for the top layer, compositional variations contribute to <1% of the observed small-scale density variations. This result then supports the conclusion that variations in porosity are the dominant factor driving the small-scale density variations in the near surface.

4.4. Discrete vs continuous density variations

We next investigate whether the density anomalies are in the form of smoothly varying density anomalies, or discrete density anomalies, such as large (relative to the model resolution) bodies of intrusions, noritic anorthosite, or buried porous materials such as impact ejecta. Because the density inversion approach we have employed only recovers smoothly varying density anomalies, we must compare our inversions of the GRAIL data to density models derived from inversions of synthetic models. For this analysis, we again consider only the upper 20 km, since the inversions are not sensitive to small-scale anomalies at greater depths. Three different sets of inversions are compared. The first density model is the inverse solution to the gravity predicted by continuous and normally distributed random densities from Section 3.3. The second density model begins with the inverse solution to the gravity field predicted by a related density forward model, but this continuous density model is discretized by setting all positive density anomalies to be +150 kg/m^3, and setting all negative density anomalies to be -150 kg/m^3. The last density model is the inversion result for area 1.

We first compared the histograms of the three different data sets (Fig. 13), and used the statistical program R to perform the Shapiro-Wilks test for normality using a p-value threshold of 0.05 (Shapiro and Wilk, 1965). The p-value is the probability of obtaining a result is equal to or

more extreme than what is actually observed given the null hypothesis that the data is normal, and we reject the null hypothesis for p-values less than 0.05. The models were also compared using a normal probability plot (Fig. 14), which is a special case of the quantile-quantile plot (or "q-q plot"). In this plot the quantiles (the data divided into bins equally spaced for a perfect normal distribution), are plotted against the theoretical quantiles that the data would have if the data were normal (Tamhane and Dunlop, 2000). Normally distributed data should fall on a line with a slope of 1 passing through the origin, and thus any deviations from this line implies a deviation from normality.

The histogram of the density inversion arising from the synthetic continuous density model resembles a normal distribution, as would be expected. The p-value from the Shapiro-Wilks test of 0.062 is above the 2-σ threshold of 0.05, so we fail to reject the null hypothesis of normality for this data set. The results of this inversion in the q-q plot lie very close to the expected line for a normal distribution, further supporting normal behavior.

The histogram of the inversion of the discrete density model is broader than one would expect from a normal distribution. This broader distribution might reflect the presence of two overlapping distributions with different means, as might be expected to arise for an inversion of a discrete density model. However, the histogram does not resolve two discrete peaks representing the two different densities. The p-value from the Shapiro-Wilks test is 6.2×10^{-15}, clearly low enough to reject the null hypothesis of normality, leading us to conclude that there is significant evidence of non-normal behavior in this density model. In the q-q plot, the densities do not plot on the normal line, instead resembling an S-shape, plotting above and below the line in the negative and positive quantiles, respectively. This q-q plot indicates that the distribution is deficient in the tails, consistent with the assessment of the histogram.

The histogram for the inversion of the actual data from area 1 resembles a normal distribution, though it is heavier in the tails. The p-value of 4.71×10^{-12} is well below the threshold, leading us to reject the null hypothesis of normality. In the q-q plot, the results again deviate from a normal distribution in the tails, but in the opposite sense to that found in the discrete density model. The histogram for the inversion of the actual data is heavier in the tails. This analysis does not support the presence of discrete density anomalies at the lower limit of the GRAIL resolution (~10 km). These results therefore are consistent with the previous conclusion that continuous variations in porosity are the dominant factor in explaining the small-scale density variations in the upper crust of the Moon. However, this analysis does not, by itself, rule out the presence of discrete anomalies on scales smaller than the gravity can resolve (e.g., variations in porosity or composition at scales much less than 10 km).

This test shows that for the scale of the density anomalies supported by the inversions, the data and inversions favor continuous rather than discrete density anomalies. Conceptually, for subsurface sources with a horizontal scale comparable to the observed gravity anomalies with a density contrast compatible with intrusions into the crust, the histogram of the modeled density anomalies should be heavier in the tails than a normal distribution. Although we cannot rule out the possibility that models of discrete anomalies could be generated that would match the data equally well, this test favors continuous and smoothly varying density variations.

5. Conclusions

High-resolution GRAIL gravity data show a ~98% correlation in the power with topography at short wavelengths (Zuber et al., 2013b). The longer wavelength Bouguer gravity anomalies correspond with variations deeper in the lunar interior, and have been used for crustal

thickness modeling (Wieczorek et al., 2013), while the shorter wavelengths must arise at depths shallower than the crust-mantle interface. Most of these short-wavelength Bouguer gravity signatures show little correlation to topographic features, with the exception of some small-scale anomalies that are correlated with basin rings or other discrete features. In this study we focused on these small-scale anomalies as an important geologic signal, rather than as noise, as they are commonly treated.

Continuous density inversion with Tikhonov regularization (Li and Oldenburg, 1996, 1998) was used to model these small-scale density variations in the lunar crust by inverting the gravity anomalies in order to solve for the underlying variations in density. A set of test cases using both previously studied lunar structures and synthetic data demonstrate that the inversion model is sensitive to both small-scale density anomalies in the top 20 km of the crust and large-scale anomalies at the crust-mantle interface.

Inversions were performed on three different small areas on the Moon, chosen because they show no clear topographic features, such as impact basins, which would dominate the gravity anomalies. The solutions reveal pervasive density variations of approximately ±100-200 kg/m^3 with characteristic length scales of 10's of km. The derived best-fit density models were used to test possible sources of these small-scale density variations, including variations in porosity, intrusions, and bulk crustal composition.

If we assume that all variations in density are due to changes in porosity alone, the inversion results predict variations in porosity from ~6% to ~19%, which is consistent with the range of porosities observed in the lunar samples (Kiefer et al., 2012a). If we assume that all variations in density in the subsurface are due to compositional variations between ferroan anorthosite and anorthositic norite or noritic anorthosite, the data require noritic anorthosite

fractions around 100% for area 3 and values greater than 100% for areas 1 and 2. All areas greatly exceed 100% if accounting for the imperfect recovery of the density model, indicating that variations in primary crustal composition cannot account for all of the observed small-scale gravity anomalies. Finally, if we assume that all variations in density are due to intrusions into the crust, we calculate a fractional volume of gabbroic intrusions no more than 50%, only slightly exceeding the expected range of 15-45% (Crites and Lucey, 2015), though greater intrusion fractions are required if we account for the imperfect recovery of the magnitude of the anomalies in the inversion. Thus, the small-scale gravity anomalies revealed by GRAIL may be a result of variations in porosity, intrusion fraction, or bulk crustal composition, but only porosity variations can account for the full magnitude of the anomalies alone. A combination of all three sources is likely. The density model solution for one area was compared to synthetic data sets representing continuous and discrete density anomalies, finding that the density anomalies depart from a normal distribution, but do not match expectations for large-scale discrete anomalies. Thus, the sources of the density anomalies are continuous and smoothly varying at the scale of the GRAIL gravity resolution (~10 km).

An analysis of the floors of the Imbrium and SP-A basins has shown that the density variations observed elsewhere on the Moon are persistent in the basin floors, leading to the conclusion that the small-scale density variations were emplaced (or continued to be emplaced) after the formation of these basins. The somewhat larger variability in density found within the high-density crust on the floor of the SP-A basin suggests that variations in porosity may be the dominant factor in formation of the small-scale density anomalies. Furthermore, a comparison between surface composition inferred from remote sensing and the density inversion results for the non-descript areas in the highlands found that variations in the abundances of minerals

indicative of high density can only explain a small fraction (<1%) of the density anomalies. Therefore, we conclude that the small-scale density variations are dominated by variations in porosity, though remote sensing data indicates that composition also plays a small role.

We acknowledge that gravity inversions are non-unique and sensitive to β, and though we have chosen a certain tradeoff between model norm and model smoothness as an optimal model, models with a different tradeoff (smaller or larger β) may also be valid. As a result the range in porosity can be stretched to beyond what is observed in lunar samples, or the predicted ranges in the fractional volume of basalt and compositional variations can be compressed to explain all the density variations. Yet our conclusion from the inversion modeling in section 4 that variations in porosity are the dominant factor in explaining the small-scale gravity inversions are supported by the basin floor models and remote sensing analyses.

We emphasize that three-dimensional density inversions based on gravity data are under-constrained and the results are non-unique. Although it may not be possible (or correct) to uniquely ascribe a single source to these gravity anomalies, we have endeavored to test different possible interpretations to the best of our abilities given available methodologies. While the model results are sensitive to assumptions, such as choice in β and weighting parameters in the inversion, all of our approaches favor porosity as the dominant source, though we feel it likely that each of the end-members tested contributes to some extent. More importantly, these analyses have revealed the existence and placed constraints on the magnitude of pervasive small-scale density variations in the upper crust of the Moon.

This study has shown that, not only does lunar crustal density vary systematically with depth and on large horizontal length scales (Besserer and Nimmo, 2013; Wieczorek et al., 2013), but it also varies horizontally and vertically on small ~10-km scales. These variations are the

dominant signal in the high-degree component of the GRAIL Bouguer gravity data, and are important to consider when interpreting the lunar gravity field. These small-scale variations are frequently treated as noise, but these variations are real and should not be neglected when investigating localized problems. This small-scale variability is important to take into account in error analysis. In particular, studies focusing on structures with dimensions of ~10-100 km (or spherical harmonic degrees greater than ~80) with density anomalies on the order of ±200 kg/m^3 may be frustrated by this background variability. Such potential target structures include dikes, lava tubes, buried craters, magma chambers, and faults. For structures at these scales, an absence of evidence in the gravity data cannot be taken as evidence for the absence of the structures. At the same time, gravity anomalies arising from this random small-scale variability could be misattributed to discrete subsurface structures (e.g., a negative or positive anomaly beneath a crater could simply be a part of this background variability with no relation to the crater). One approach to circumvent this limitation is by using large numbers of structures (e.g., Soderblom et al., 2015; Bierson et al., 2016) or averaging along lines or axes of symmetry (e.g., Andrews-Hanna et al., 2013).

In addition to acting as "noise" for studies of discrete surface structures, this small-scale density variability is an important signal in itself. These variations are an indication that many more processes are (or have been) operating in the lunar crust than those reflected in the surface geology alone. The timing of the formation of these small-scale variations appears to postdate the formation of the major impact basins on the Moon, but to largely predate the emplacement of the majority of the basin-filling maria. Cratering provides one ongoing mechanism for generating this heterogeneity (Milbury et al., 2015), though a study of the gravity signal of complex craters found the scatter about the trend to be greater than the crater signal

itself at small diameters (<100 km) (Soderblom et al., 2015). However, the net effect of the long history of impact cratering on the Moon was likely the generation of a complex heterogeneous crust, consisting of discrete zones of impact melt, ejecta, and fractured and brecciated rocks.

The GRAIL mission has given us high-resolution gravity data exceeding expectations, allowing us to investigate density variations on scales much smaller than can be resolved on other planets. The other terrestrial planets have experienced equally complex histories of processes affecting their surfaces and interiors, and thus are likely similarly heterogeneous. Previous work has shown variability on large scales of 100-1000's of km (Besserer and Nimmo, 2013; Wieczorek et al., 2013). Here we show that variability exist on the smallest scales resolved by GRAIL of 10's of km. From lunar samples we know that there is variability on the smaller scales of 10's of cm and smaller, as well. The density anomalies at all scales ranging from centimeters to 1000's of km are comparable in magnitude. Although the assumption of uniform density in analyses of structures on the Moon and other planets is often a necessary simplification, it must be recognized that this assumption is invariably incorrect. This density variability has a substantial impact on any interpretations of planetary gravity data, across all scales.

Acknowledgements. This work was supported by grants to JCAH from the NASA GRAIL Guest Scientist Program and the NASA Lunar Data Analysis Program. We are grateful to Greg Neumann and an anonymous reviewer for comments their thoughtful reviews. The GRAIL mission is a component of the NASA Discovery Program and is performed under contract to the Massachusetts Institute of Technology and the Jet Propulsion Laboratory, California Institute of Technology.

References.

Andrews-Hanna, J. C., 2013, The origin of the non-mare mascon gravity anomalies in lunar basins, Icarus 222, 159–168, doi:10.1016/j.icarus.2012.10.031.

Andrews-Hanna, J. C., Asmar, S. W., Head, J. W., Kiefer, W. S., Konopliv, A. S., Lemoine, F. G., Matsuyama, I., Mazarico, E., McGovern, P. J., Melosh, H. J., Neumann, G. A., Nimmo, F., Phillips, R. J., Smith, D. E., Solomon, S. C., Taylor, G. J., Wieczorek, M. A., Williams, J. G., Zuber, M. T., 2013. Ancient igneous intrusions and early expansion of the Moon revealed by GRAIL gravity gradiometry. Science 339, 675–678. doi:10.1126/science.1231753.

Besserer, J., Nimmo, F., 2013. Theoretical and observational constraints on Lunar mega-regolith thickness. Lunar and Plant. Sci. Conf., 2463.

Besserer, J., Nimmo, F., Wieczorek, M. A., Weber, R. C., Kiefer, W. S., McGovern, P. J., Andrews-Hanna, J. C., Smith, D. E., Zuber, M. T., 2014. GRAIL gravity constraints on the vertical and lateral structure of the lunar crust. Geophys. Res. Lett. 41, 16, 5771-16,5777. doi: 10.1002/2014GL060240.

Bierson, C. J., Phillips, R. J., Nimmo, F., Besserer, J., Milbury,C., Keane, J. T., Soderblom, J. M., and Zuber, M. T., 2016. Interactions between complex craters and the lunar crust: Analysis using GRAIL data. J. Geophys. Res. Planets, 121, 1488-1497. doi: 10.1002/2016JE005090.

Cashore, J., Woronow, A., 1985. A new Monte Carlo model of Lunar regolith development. J. Geophys. Res., 90, S02, C811-C815.

Cheek, L. C., Donaldson Hanna, K. L., Pieters, C. M., Head, J. W., Whitten, J. L., 2013. The distribution and purity of anorthosite across the Orientale basin: New perspectives from

Moon Mineralogy Mapper data. J. Geophys. Res. Planets 118, 1-16. doi:10.1002/jgre.20126.

Crites, S. T., Lucey, P. G., 2015. Revised mineral and Mg# maps of the Moon from integrating results from the Lunar Prospector neutron and gamma-ray spectrometers with Clementine spectroscopy. Am. Mineral. 100, 973-982. doi:10.2138/am-2015-4874.

Dymek, R. F., Albee, A. L., Chodos, A. A., 1976. Petrology and origin of Boulders no. 2 and no. 3, Apollo 17 Station 2. Proc Lunar Sci Conf., 2335–2378.

Freed, A. M., Johnson, B. C., Blair, D. M., Melosh, H. J., Neumann, G. A., Phillips, R. J., Solomon, S. C., Wieczorek, M. A., and Zuber, M. T., 2014. The formation of lunar mascon basins from impact to contemporary form, J. Geophys. Res. Planets, 119, 2378–2397. doi:10.1002/2014JE004657.

Gong, S., Wieczorek, M. A., Nimmo, F., Kiefer, W. S., Head, J. W., Huang, C., Smith, D. E., and Zuber, M. T., 2016. Thickness of mare basalts on the Moon from gravity and topography. J. Geophys. Res. Planets, 121, 854-870. doi: 10.1002/2016JE005008.

Han, S-C, Schmerr, N., Neumann, G. A., Holmes, S., 2014. Global characterictics of porosity and density stratiffication within the Lunar crust from GRAIL gravity and Lunar Orbiter Laser Altimeter topography data. Geophys. Res. Lett. 41, 1882-1889, doi: .10.1002/2014GL059378.

Hansen, P. C., 1992. Analysis of discrete ill-posed problems by means of the L-curve, SIAM Review, 34(4), pp. 561-580.

Hawke, B. R., Peterson, C. A., Blewett, D. T., Bussey, D. B. J., Lucey, P. G., Taylor, G. J., Spudis, P. D., 2003. Distribution and modes of occurrence of lunar anorthosite. J. Geophys. Res. 108, 5050. doi:10.1029/2002JE001890.

Head J. W. III, and Wilson, L., 1992. Lunar mare volcanism: Stratigraphy, eruption conditions, and the evolution of secondary crusts, Geochimica et Cosmochimica Acta 55, 2155-2175.

Head, J. W., and Wilson, L., 1993. Lunar graben formation due to near-surface deformation accompanying dike emplacement. Planet. Space Sci. 41, 10, 719-727. doi: 10.1016/0032-0633(93)90114-H.

Huang, Q., and Wieczorek, M. A., 2012. Density and porosity of the lunar crust form gravity and topography. J. Geophys, Res. 117, E05003, doi: 10.1029/2012JE004062

Jozwiak, L. M., Head, J. W., Zuber, M. T., Smith, D. E., Neumann, G. A., 2012. Lunar floor-fractured craters: Classification, distribution, origin and implications for magmatism and shallow crustal structure. J. Geophys. Res. 117, E11005. doi:10.1029/2012JE004134.

Jozwiak, L. M., Head, J. W., and Wilson, L., 2015. Lunar floor-fractured craters as magmatic intrusions: Geometry, modes of emplacement, associated tectonic and volcanic features, and implications for gravity anomalies, Icarus 248, 424-447, doi: 10.1016/j.icarus.2014.10.052.

Jozwiak, L.M., Head, J.W., Neumann, G.A. and Wilson, L., 2016. Observational Constraints on the Identification of Shallow Lunar Magmatism: Insights from Floor-fractured Craters. Icarus, online available article. doi: 10.1016/j.icarus.2016.04.020.

Kattoum, Y. N., Andrews-Hanna, J. C., 2013. Evidence for ring-faults around the Orientale basin on the Moon from gravity. Icarus 226, 694–707. doi:10.1016/j.icarus.2013.06.025.

Kiefer, W. S., Macke, R. J., Britt, D. T., Irving, A. J., Consolmagno, G. J., 2012a. The density and porosity of lunar rocks. Geophys. Res. Lett. 39, L07201. doi:10.1029/2012GL051319.

Kiefer, W. S., Macke, R. J., Britt, D. T., Irving, A. J., and Consolmagno, G. J., 2012b. Density and porosity of lunar feldspathic Rocks and implications for lunar gravity modeling. Sec. Conf. Lunar High. Crust, #9006.

Kiefer, W. S., 2013. Gravity constraints on the subsurface structure of the Marius Hills: The magmatic plumbing of the largest lunar volcanic dome complex. J. Geophys. Res. Planets 118, 1-13. doi:10.1029/2012JE004111.

Konopliv, A. S., Park, R. S., Yuan, D., Asmar, S. W., Watkins, M. M., Williams, J. G. Fahnestock, E., Kruizinga, G., Paik, M., Strekalov, D., Harvey, N., Smith, D. E., Zuber, M. T., 2014. High-resolution lunar gravity fields from the GRAIL Primary and Extended Missions. Geophys. Res. Lett. 41, 1452-1458, 10.1002/2013GL059066.

Lemoine, F. G., Goossens, S., Sabaka, T. J., Nicholas, J. B., Mazarico, E., Rowlands, D. D., Loomis, B. D., Chinn, D. S., Neumann, G. A., Smith, D. E., Zuber, M. T., 2014. GRGM900C: A degree 900 lunar gravity model from GRAIL primary and extended mission data. Geophys. Res. Lett. 41, 10, 3382 - 3389. doi:10.1002/2014GL060027.

Li, Y., Oldenburg, D. W., 1996. 3-D inversion of magnetic data. Geophysics 61, 2, 394–408. doi: 10.1190/1.443968.

Li, Y., Oldenburg, D. W., 1998. 3-D inversion of gravity data. Geophysics 63,1, 109–119. doi: 10.1190/1.44302.

Liang, Q., Chen, C., Li, Y., 2014. 3-D inversion of gravity data in spherical coordinates with application to the GRAIL data. J. Geophys. Res. Planets 119, 1359–1373. doi:10.1002/2014JE004626.

Longhi, J., 2003. A new view of lunar ferroan anorthosites: postmagma ocean petrogenesis. J. Geophys. Res. 108, 5083. doi:10.1029/2002JE001941, E8.

Lucey, P. G., 2004. Mineral maps of the Moon. Geophys. Res. Lett. 31, L08701, doi:1029/2003GL019406.

Melosh, H. J., Freed, A. M, Johnson, B. C., Blair, D. M., Andrews-Hanna, J. C., Neumann, G. A., Phillips, R. J, Smith, D. E., Solomon, S. C., Wieczorek, M. A., Zuber, M. T, 2013. The origin of lunar mascon basins. Science 340, 1552-1555. doi: 10.1126/science.1235768.

Milbury, C., Johynson, B. C., Melosh, H. J., Colins, G. S., Blair, D. M., Soderblom, J. M., Nimmo, F., Bierson, C. J., Phillips, R. J., Zuber, M. T., 2015. Pre-Impact Porosity Controls the Gravity Signature of Lunar Craters. Geophys. Res. Lett., 42, 9711–9716, doi:10.1002/2015GL066198.

Namiki, N., Iwata, T., Matsumoto, K., Hanada, H., Noda, H., Goossens, S., Ogawa, M., Kawano, N., Asari, K., Tsuruta, S.-I., Ishihara, Y., Liu, Q., Kikuchi, F., Ishikawa, T., Sasaki, S., Aoshima, C., Kurosawa, K., Sugita, S., Takano, T., 2009. Farside gravity field of the moon from four-way Doppler measurements of SELENE (Kaguya). Science 323, 900–905. doi:10.1126/science.1168029.

Neumann, G. A., Zuber, M. T., Smith, D. E., Lemoine, F. G., 1996. The lunar crust: Global structure and signature of major basins. J. Geophys. Res. 101, E7, 16,841-16,863. doi: 10.1029/96JE01246.

Neumann, G. A., Zuber, M. T., Wieczorek, M. A., Head, J. W., Baker, D. M. H., Solomon, S. C., Smith, D. E., Lemoine, F. G., Mazarico, E., Sabaka, T. J., Goossens, S. J., Melosh, H. J., Phillips, R. J., Asmar, S. W., Konopliv, A. S., Williams, J. G., Sori, M. M., Soderblom, J. M., Miljković, K., Andrews-Hanna, J. C., Nimmo, F., Kiefer, W. S., 2015. Lunar impact basins revealed by Gravity Recovery and Interior laboratory measurements. Sci. Adv. 2015, 1(9), e1500852, doi:10.1126/sciadv.1500852.

Ohtake, M., Matsunaga, T., Haruyama, J., Yokota, Y., Morota, T., Honda, C., Ogawa, Y., Torii, M., Miyamoto, H., Arai, T., Hirata, N., Iwasaki, A., Nakamura, R., Hiroi, T., Sugihara, T., Takeda, H., Otake, H., Pieters, C. M., Saiki, K., Kitazato, K., Abe, M., Asada, N., Demura, H., Yamaguchi, Y., Sasaki, S., Kodama, S., Terazono, J., Shirao, M., Yamaji, A., Minami, S., Akiyama, H., Josset, J.-L., 2009. The global distribution of pure anorthosite on the Moon. Nature 461, 236–240. doi:10.1038/nature08317.

Papike, J.J., Ryder, G., Shearer, C.K., 1998. Lunar samples. Min. Soc. Am., Planetary Materials 36, 5.001–5.234.

Pieters, C. M., Boardman, J., Buratti, B., Clark, R., Combe, J.-P., Green, R., Goswami, J. N., Head, J. W., Hicks, M., Isaacson, P., Klima, R., Kramer, G., Kumar, S., Lundeen, S., Malaret, E., McCord, T. B., Mustard, J., Nettles, J., Petro, N., Runyon, C., Staid, M., Sunshine, J., Taylor, L., Tompkins, S., Varanasi, P., 2009. Mineralogy of the lunar crust in spatial context: First results from the moon mineralogy mapper (M3). Lunar and Plan. Sci. Conf. p. 2052.

Prettyman, T. H., Hagerty, J. J., Elphic, R. C., Feldman, W. C., Lawrence, D. J., McKinney, G. W., Vaniman, D. T., 2006. Elemental composition of the lunar surface: Analysis of gamma ray spectroscopy data from Lunar Prospector. J. Geophys. Res. 111, E12007. doi:10.1029/2005JE002656.

Prissel, T. C., Parman, S. W., Jackson, C. R. M., Rutherford, M. J., Hess, P. C., Head., J. W. III, Cheek, L. C., Dhingra, D., and Pieters, C. M., 2014. Pink Moon: The petrogenesis of pink spinel anorthosites and implications concerning Mg-suite magmatism, Earth Planet. Sci. Lett., 403 144-156, doi: 10.1016/j.epsl.2014.06.027.

Shapiro, S. S., Wilk, M. B., 1965. An Analysis of Variance Test for Normality (Complete Samples). Biometrika 52, 591–611. doi:10.1093/biomet/52.3-4.591.

Smith, J. V., Anderson, A. T., Newton, R. C., Olsen, E. J., Wyllie, P. J., Crewe, A. V., Isaacson, M. S., Johnson, D., 1970. Petrologic history of the moon inferred from petrography, mineralogy, and petrogenesis of Apollo 11 rocks. Apollo 11 Lun. Sci. Conf. 1, 897–925

Soderblom, J. M., Evans, A. J., Johnson, B. C., Melosh, H. J., Miljković, K., Phillips, R. J., Andrews-Hanna, J. C., Bierson, C. J., Head, J. W., Milbury, C., Neumann, G. A., Nimmo, F., Smith, D. E., Solomon, S. C., Sori, M. M., Wieczorek, M. A., Zuber, M. T., 2015. The fractured Moon: Production and saturation of porosity in the lunar highlands from impact cratering. Geophys. Res. Lett., 42 6939-6944, doi:10.1002/2015GL065022.

Solomon, S. C. and Head, J. W., 1980. Lunar mascon basins: Lava filling, tectonics, and evolution of the lithosphere. Rev. Geophys. Space Phys., 18, 1, 107-141.

Sori, M. M., Zuber, M. T., Head, J. W. III, and Kiefer, W. S., 2016. Gravitational search for cryptovolcanism on the Moon: Evidence for large volumes of early igneous activity. Icarus, 273, 284–295. doi: 10.1016/j.icarus.2016.02.009.

Spudis, P. D., Martin, D. J. P., Kramer, G., 2014. Geology and composition of the Orientale Basin impact melt sheet. J. Geophys. Res. Planet. 119, 19-29, doi:10.1002/2013JE004521.

Tamhane, A. C., Dunlop, D. D., 2000. Statistics and data analysis, from elementary to intermediate. Prentice Hall.

Thorey, C., Michaut, C., Wieczorek, W., 2015. Gravitational signatures of lunar floor-fractured craters. EPSL 424, 269-279.

Vaughan, W. M., Head, J. W. III, Wilson, L., Hess, P. C., 2013. Geology and petrology of enromous volumes of impact melt on the Moon: A case study of the Orientale basin impact melt sea. Icarus 223, 749-765.

Vaughan W. M., Head, J. W. III, 2014. Impact melt differentiation in the South Pole-Aitken basin: Some observations and speculations, Planet. Space Sci. 91, 101-106, doi: 10.1016/j.pss.2013.11.010.

Warren, P. H., Wasson, J. T., 1977. Pristine nonmare rocks and the nature of the lunar crust. Proc. Lunar Sci. Conf., 8th, 2215–2235.

Warren, P. H., Wasson, J. T., 1979. The origin of KREEP. Rev. Geophys. Space Phys., 17, 1, 73–88. doi:10.1029/RG017i001p00073.

Warren, P. H., 1985. The magma ocean concept and lunar evolution. Ann. Rev. Earth Planet. Sci., 13, 201-40. doi:10.1146/annurev.earth.13.1.201.

Warren, P. H., 1990. Lunar anorthosites and the magma-ocean plagioclase-flotation hypotheses: importance of FeO enrichment in the parent magma. Am. Mineral. 75, 46-58.

Warren, P. H., 1993. A concise compilation of petrologic information on possibly pristine nonmare Moon rocks. Am. Mineral. 78, 360–376.

Whitten, J. L., and Head., J. W. III, 2013. Detecting volcanic resurfacing of heavily cratered terrain: Flooding simulations on the Moon using Lunar Orbiter Laser Altimeter (LOLA) data, Planet. Space Sci. 85, 24-37, doi: 10.1016/j.pss.2013.05.013.

Whitten, J. L., and Head., J. W. III, 2015a. Lunar cryptomaria: Physical characteristics, distribution, and implications for ancient volcanism, Icarus 247, pp. 150-171, doi: 10.1016/j.icarus.2014.09.031.

Whitten, J. L., and Head., J. W. III, 2015b. Lunar cryptomaria: Mineralogy and composition of ancient volcanic deposits, Planet. Space Sci. 106, pp. 67-81, doi: 10.1016/j.pss.2014.11.027.

Wieczorek, M. A., Phillips, R. J., 1998. Potential anomalies on a sphere: Applications to the thickness of the lunar crust. J. Geophys. Res. 103, E1, 1715–1724.

Wieczorek, M. A., Jolliff, B. L., Khan, A., Pritchard, M. E., Weiss, B. P., Williams, J. G., Hood, L. L., Righter, K., Neal, C. R., Shearer, C. K., McCallum, I. S., Tompkins, S., Hawke, B. R., Peterson, C., Gillis, J. J., Bussey, B., 2006. The Constitution and Structure of the Lunar Interior. Rev. Mineral. Geochem. 60, 221–364. doi:10.2138/rmg.2006.60.3.

Wieczorek, M. A., Neumann, G. A., Nimmo, F., Kiefer, W. S., Taylor, G. J., Melosh, H. J., Phillips, R. J., Solomon, S. C., Andrews-Hanna, J. C., Asmar, S. W., Konopliv, A. S., Lemoine, F. G., Smith, D. E., Watkins, M. M., Williams, J. G., Zuber, M. T., 2013. The crust of the Moon as seen by GRAIL. Science 339, 671–675. doi: 10.1126/science.1231530.

Wieczorek, M. A., 2014. SHTOOLS - Tools for working with spherical harmonics (v2.9.1). Zenodo. 10.5281/zenodo.12158.

Wood, J. A., Dickey, J. S., Marvin, U. B., Powell, B. N., 1970. Lunar anorthosites and a geophysical model of the moon. Apollo 11 Sci. Conf. 1, 965–988.

Zuber, M.T., D.E. Smith, D.H. Lehman, T.L. Hoffman, S.W. Asmar and M.M. Watkins, 2013a.

Gravity Recovery and Interior Laboratory (GRAIL): Mapping the lunar interior from crust to core. Space Sci. Rev. 178, doi: 10.1007/s11214-012-9952-7.

Zuber, M. T., Smith, D. E., Watkins, M. M., Asmar, S. W., Konopliv, A. S., Lemoine, F. G., Melosh, H. J., Neumann, G. A., Phillips, R. J., Solomon, S. C., Wieczorek, M. A., Williams, J. G., Goossens, S. J., Kruizinga, G., Mazarico, E., Park, R. S., Yuan, D., 2013b. Gravity field of the Moon from the Gravity Recovery and Interior Laboratory (GRAIL) mission. Science 339, 668–671, doi: 10.1126/science.1231507.

Figures

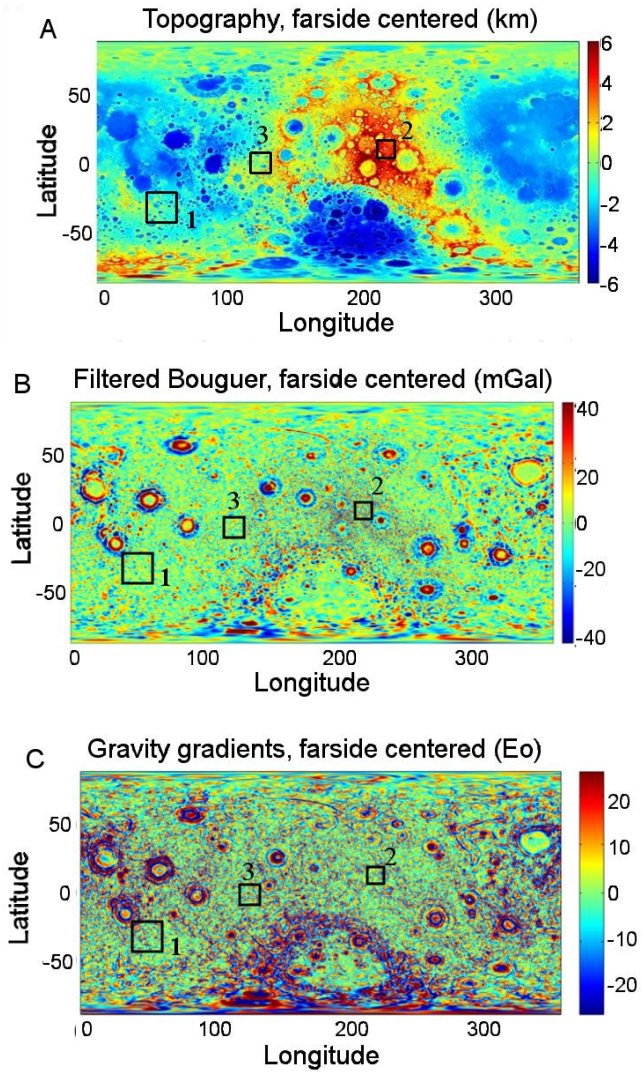

Figure 1: Global Lunar Maps. A) Topography, expanded to spherical harmonic degree 1800. B) Bouguer gravity filtered using the complementary minimum amplitude filter (see text). C) Gravity Gradient map, with a high-pass filter applied at degree 50 and a low-pass cosine filter applied from degree 350 to degree 400. The outlined boxes refer to the three study areas of figure 6.

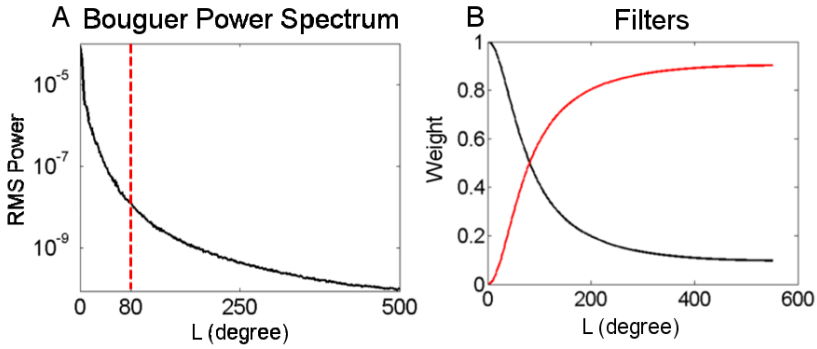

Figure 2: A) Root mean square power spectrum of GRAIL gravity model (GRGM900B_Bouguer). Red dotted line indicates the degree at which the minimum amplitude filter has a magnitude one half. B) Minimum amplitude (black; Wieczorek et al., 2013) and complementary minimum amplitude (red) filters applied to the gravity data. The complementary minimum amplitude filter was used in all analyses in this work. A low-pass filter from degree 550 to degree 600 was added to the complementary filter (not shown here) to prevent ringing.

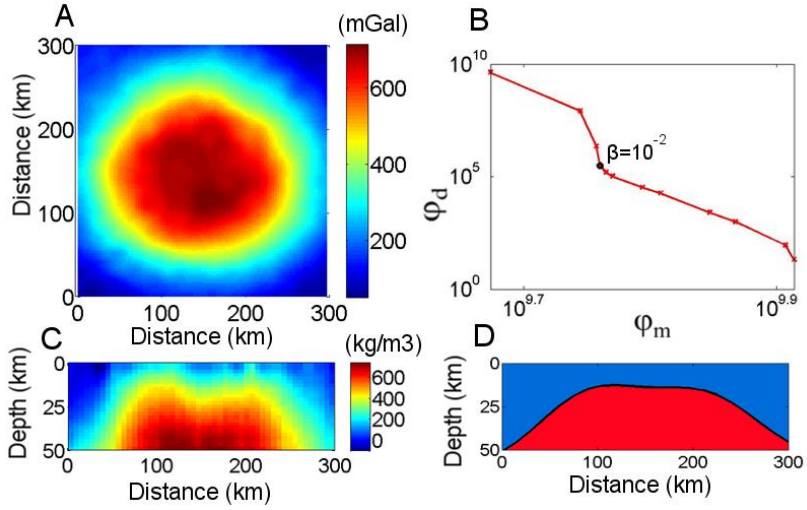

Figure 3: A) Bouguer corrected gravity anomaly of the Freundlich-Sharonov basin. B) Tikhonov curve (L-curve) with the data misfit on the y-axis and the model norm on the x-axis. The β values vary from left to right on the curve in increments of a factor of 10. C) Cross-section of the

optimal density model indicated by the black circle in B). D) Cross-section through the crustal thickness model of the same location in C).

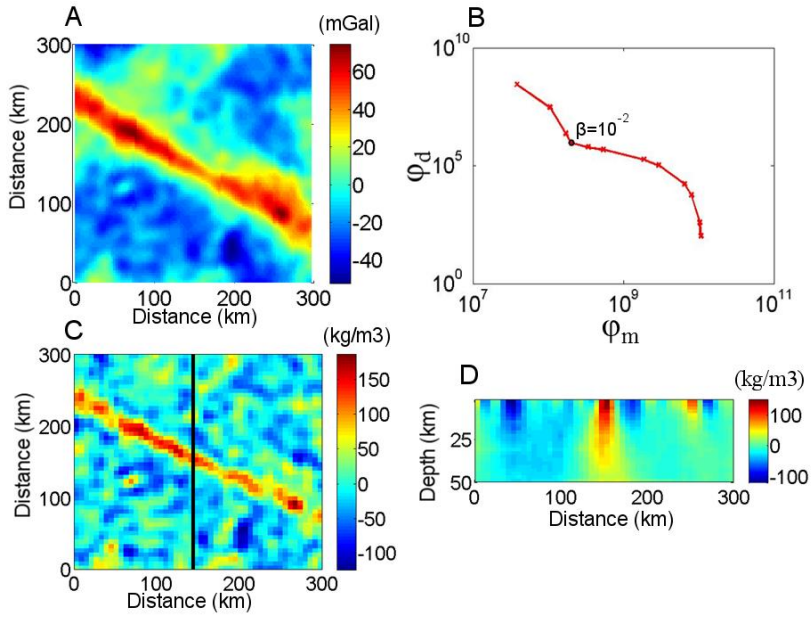

Figure 4: A) Bouguer corrected gravity anomaly of linear feature 1 from Andrews-Hanna et al. (2013). B) Tikhonov curve (or L-curve). The β values vary from left to right on the curve in increments of a factor of 10. C) Horizontal cross-section through the optimal density model solution indicated by the black circle in B), at 10 km depth. D) Vertical cross-section through the density model in C) at the location of the black line.

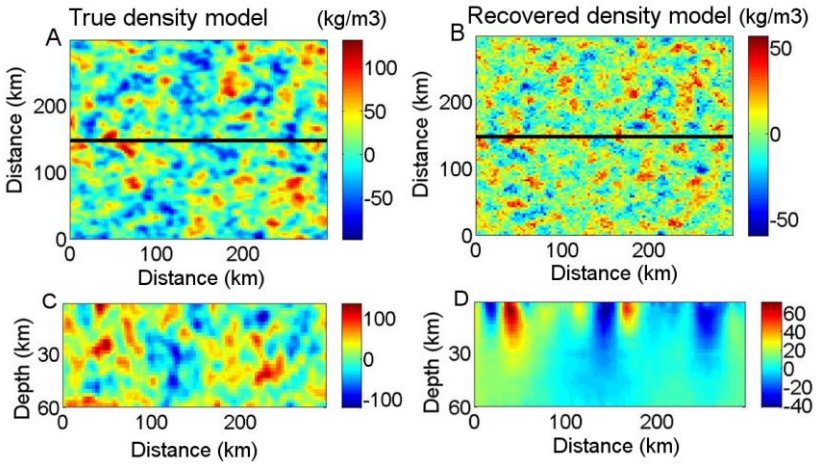

Figure 5: Inversion results of gravity data derived from a synthetic density model. Panels A and B are horizontal planar sections of the synthetic and recovered density model, respectively, at depths of 10 km. Bottom panels C and D are vertical cross-sections located at the black lines in A and B of the synthetic and recovered density model, respectively.

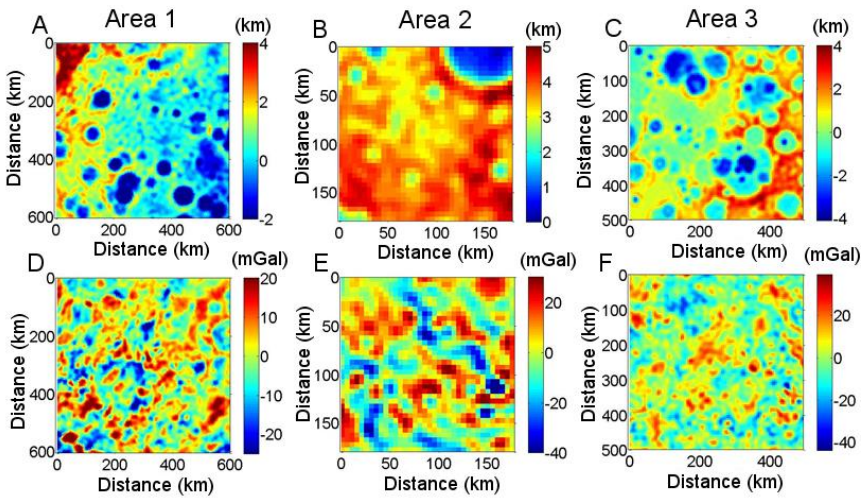

Figure 6: Topography (A-C) and Bouguer gravity (D-F) maps of non-descript areas (locations indicated in Fig. 1). Gravity data was filtered with the complementary minimum amplitude filter.

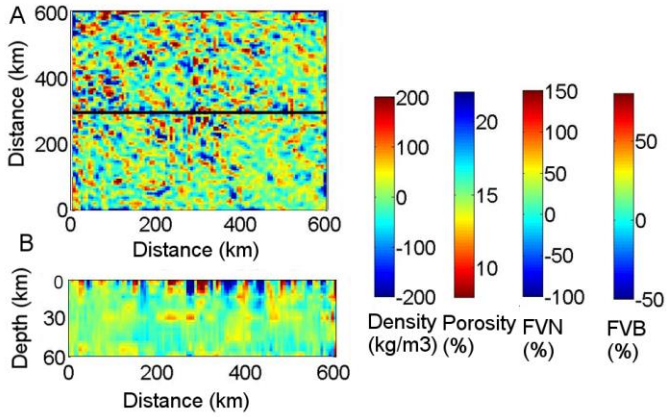

Figure 7: Optimal inversion result for non-descript Area 1. The horizontal cross-section (A) is taken at 2 km depth, and the vertical cross-section (B) is taken at the location of the black line in A. The color bars each refer to a different analysis of the solution. FVN indicates the change in

composition of the bulk lunar crust as represented by the fractional volume of noritic anorthosite, FVB indicates the fractional volume of a basaltic intrusion into the crust.

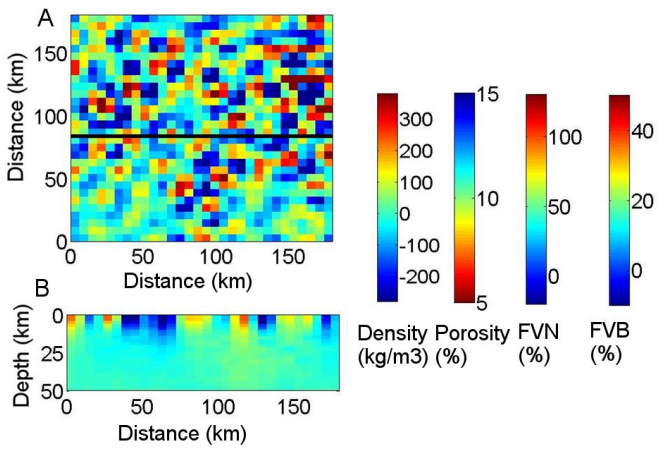

Figure 8: Optimal inversion result for non-descript Area 2 (details are the same as Fig. 7).

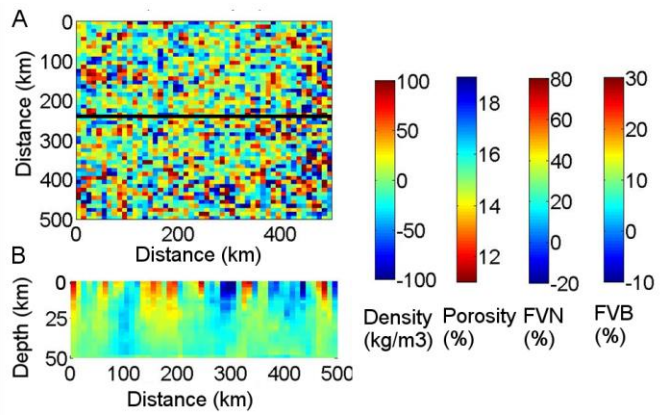

Figure 9: Optimal inversion model for non-descript Area 3 (details are the same as Fig. 7).

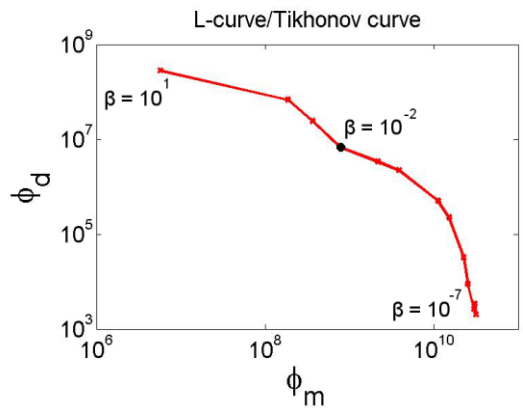

Figure 10: Tikhonov/L-curve for area 3. The optimal β for this area is the knee point where $\beta=10^{-2}$ and the two extremes are also indicated.

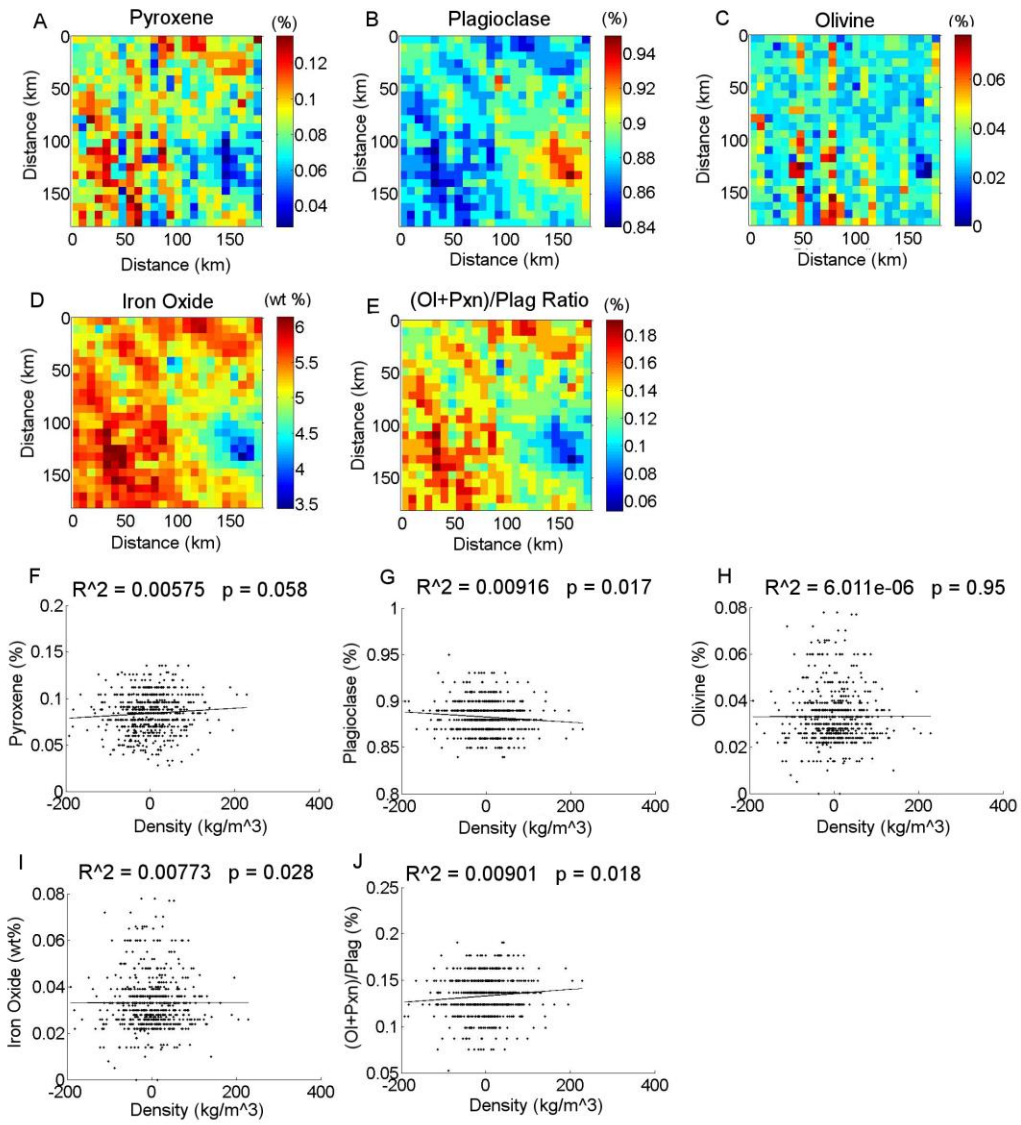

Figure 11: (A-E) Mineral abundance maps derived from remote sensing data for Area 2 of pyroxene, plagioclase, olivine, iron oxide, and a (olivine+pyroxene)/plagioclase ratio, respectively. (F-J) The corresponding scatter plots, showing the best-fit line along with the associated the p-values and R^2 values.

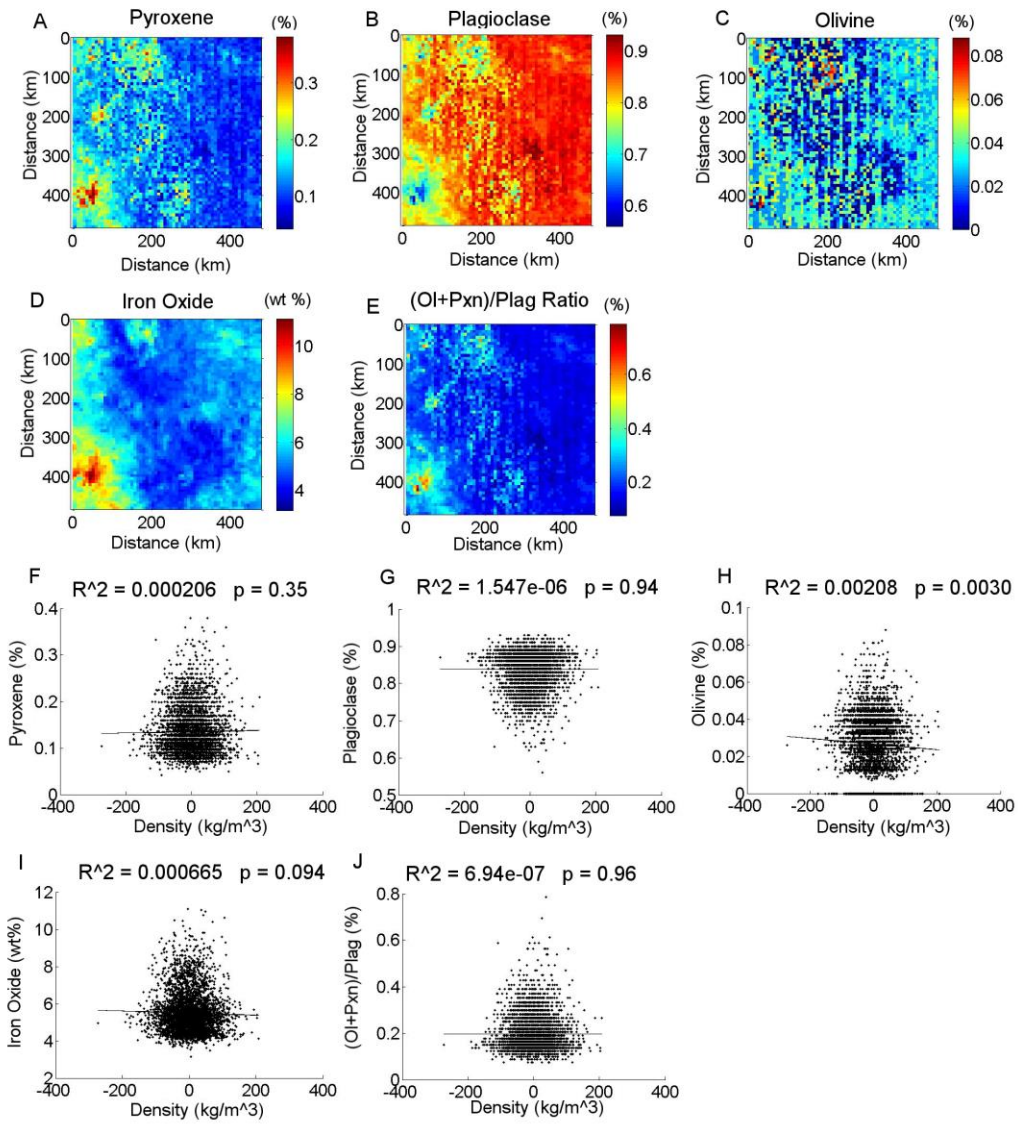

Figure 12: Same as Fig. 11, but for Area 3.

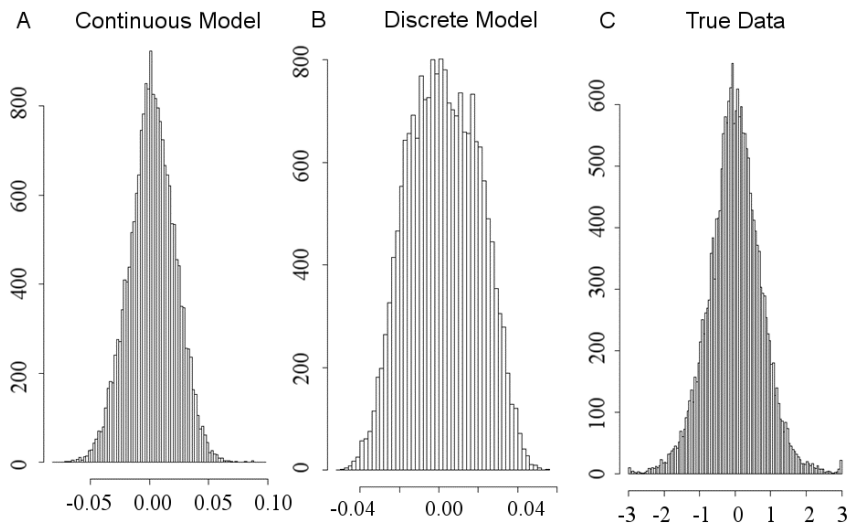

Figure 13: Histograms of the density inversions derived from the continuous density anomaly forward model (A), the discrete density anomaly forward model (B), and the GRAIL data over the non-descript area (C).

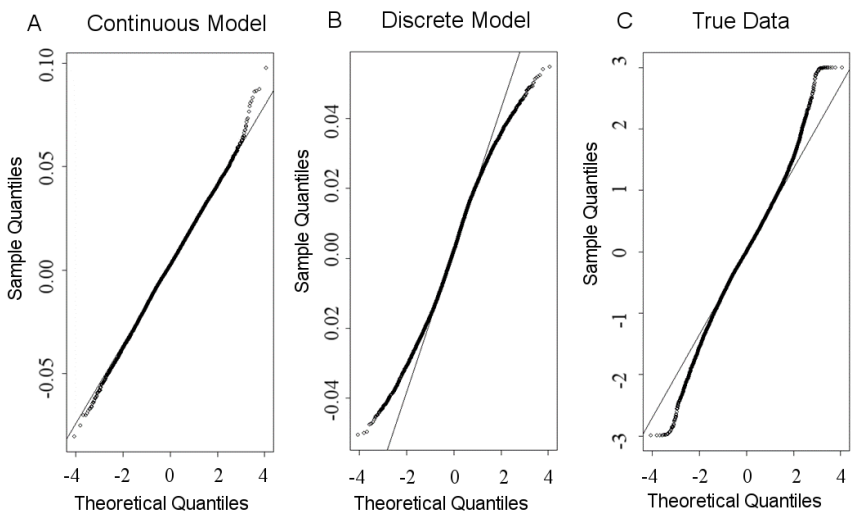

Figure 14: Normal probability quantile-quantile (QQ) plots of the density inversions of the synthetic gravity from the continuous (A) and discrete (B) density models, and of the true gravity data (C). The thin line in each panel represents a normal distribution.

	Density anomaly (kg/m^3)	*Porosity (%)*	*FVN (%)*	*FVB (%)*
Area 1	μ = -1.7	μ = 15.0	μ = 146.2	μ = 73.1
	σ = 110.5	σ = 3.7	σ = 73.7	σ = 36.8
Area 2	μ = -0.2	μ = 11.0	μ = 91.7	μ = 33.3
	σ = 91.8	σ = 3.1	σ = 45.9	σ = 16.7
Area 3	μ = 0.1	μ = 15.0	μ = 49.1	μ = 16.4
	σ = 49.1	σ = 1.6	σ = 24.5	σ = 8.2

Table 1: The mean and standard deviation values of the three non-descript areas for density anomaly, porosity, fractional volume of norite (FVN), and fractional volume basalt (FVB).

	Density anomaly (kg/m^3)	*Porosity (%)*	*FVN (%)*	*FVB (%)*
Area 1	μ = -2.9	μ = 15.0	μ = 243.7	μ = 121.8
	σ = 184.2	σ = 6.1	σ = 122.8	σ = 61.4
Area 2	μ = -0.4	μ = 11.0	μ = 152.8	μ = 55.6
	σ = 153.1	σ = 5.2	σ = 76.5	σ = 27.8
Area 3	μ = 0.1	μ = 15.0	μ = 81.8	μ = 27.3
	σ = 81.8	σ = 2.7	σ = 40.9	σ = 13.6

Table 2: The mean and standard deviation values of the three non-descript areas for density anomaly, porosity, fractional volume of norite (FVN), and fractional volume basalt (FVB), corrected for the assumption of only recovering 60% of the original model.

	Density anomaly (kg/m^3)	*Porosity (%)*	*FVN (%)*	*FVB (%)*
Imbrium (DC 2 km)	μ = 1.3	μ = 6.9	μ = 22.1	μ = 11.0
	σ = 15.9	σ = 0.5	σ = 10.6	σ = 5.3
Imbrium (DC 9 km)	μ = 0.0	μ = 6.1	μ = 88.0	μ = 44.0
	σ = 51.8	σ = 1.5	σ = 34.6	σ = 17.3
ND2	μ = -0.2	μ = 11.0	μ = 33.2	μ = 12.1
	σ = 33.3	σ = 1.1	σ = 16.7	σ = 6.1
-SP-A	μ = -1.2	μ = 11.0	μ = 36.9	μ = 13.4
	σ = 37.5	σ = 1.3	σ = 18.8	σ = 6.8

Table 3: The mean and standard deviation values of Imbrium, downward continued to 2 km depth and to 9 km depth, for density anomaly, porosity, fractional volume of norite (FVN), and fractional volume basalt (FVB), compared to Area 2 and a small patch on South Pole-Aitken basin.